Article

Developmental Cell

# Ribosomal RNA 2′-O-methylation dynamics impact cell fate decisions

## Graphical abstract

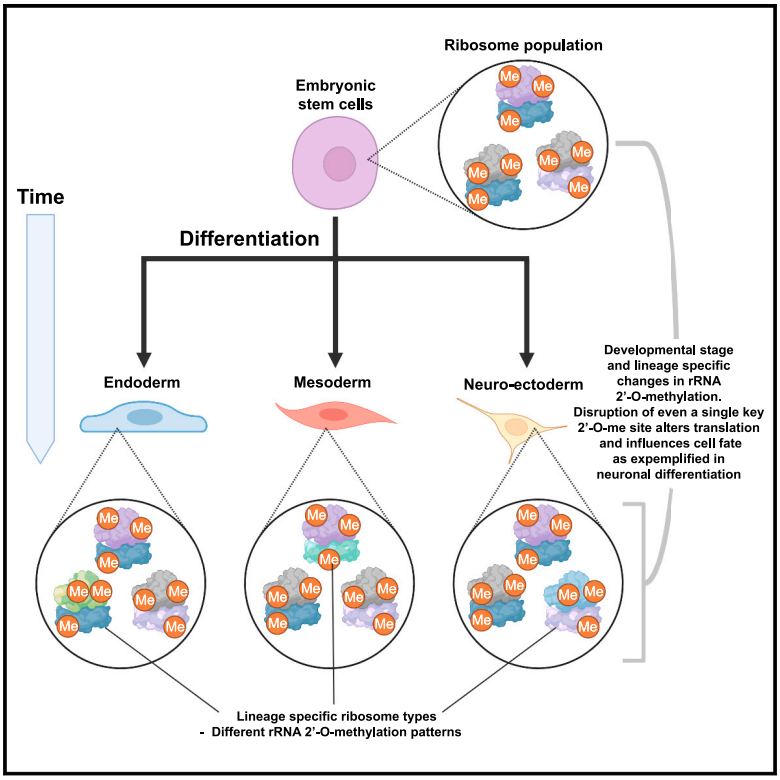


## Highlights

- rRNA modifications change during mouse brain development and hESC differentiation
- Changes to the rRNA methylation profile occur during germ layer specification
- Abrogation of methylation at 28S:U3904 impacts the translation of WNT pathway members
- Lack of methylation at 28S:U3904 shifts hESCs toward a neurectoderm fate

## Authors

Sophia J. Häfner, Martin D. Jansson, Kübra Altinel, ..., Matthew L. Kraushar, Agnete Kirkeby, Anders H. Lund

## Correspondence

sophia.hafner@bric.ku.dk (S.J.H.), anders.lund@bric.ku.dk (A.H.L.)

## In brief

Ribosomes produce one of the main building blocks of living beings—proteins—and exhibit structural variations, such as RNA methylations. Häfner et al. show that some methylations behave dynamically during cell differentiation and that their manipulation impacts cell fate decision-making.

Häfner et al., 2023, Developmental Cell *58*, 1593–1609
September 11, 2023 © 2023 Elsevier Inc.
https://doi.org/10.1016/j.devcel.2023.06.007

CellPress

Developmental Cell

CellPress

Article

# Ribosomal RNA 2′-O-methylation dynamics impact cell fate decisions

Sophia J. Häfner,[1,*] Martin D. Jansson,[1] Kübra Altinel,[1] Kasper L. Andersen,[1] Zehra Abay-Nørgaard,[2] Patrice Ménard,[1] Martin Fontenas,[1] Daniel M. Sørensen,[1] David M. Gay,[1] Frederic S. Arendrup,[1] Disa Tehler,[1] Nicolai Krogh,[3] Henrik Nielsen,[3] Matthew L. Kraushar,[4] Agnete Kirkeby,[2,5] and Anders H. Lund[1,6,*]

[1]Biotech Research and Innovation Centre, Faculty of Health and Medical Sciences, University of Copenhagen, 2200 Copenhagen, Denmark
[2]Novo Nordisk Foundation Center for Stem Cell Medicine (reNEW) and Department of Neuroscience, Faculty of Health and Medical Science, University of Copenhagen, 2200 Copenhagen, Denmark
[3]Department of Cellular and Molecular Medicine, Faculty of Health and Medical Sciences, University of Copenhagen, 2200 Copenhagen, Denmark
[4]Max Planck Institute for Molecular Genetics, 14195 Berlin, Germany
[5]Wallenberg Center for Molecular Medicine, Department of Experimental Medical Science, Lund University, 22184 Lund, Sweden
[6]Lead contact
*Correspondence: sophia.hafner@bric.ku.dk (S.J.H.), anders.lund@bric.ku.dk (A.H.L.)
https://doi.org/10.1016/j.devcel.2023.06.007

## SUMMARY

Translational regulation impacts both pluripotency maintenance and cell differentiation. To what degree the ribosome exerts control over this process remains unanswered. Accumulating evidence has demonstrated heterogeneity in ribosome composition in various organisms. 2′-O-methylation (2′-O-me) of rRNA represents an important source of heterogeneity, where site-specific alteration of methylation levels can modulate translation. Here, we examine changes in rRNA 2′-O-me during mouse brain development and tri-lineage differentiation of human embryonic stem cells (hESCs). We find distinct alterations between brain regions, as well as clear dynamics during cortex development and germ layer differentiation. We identify a methylation site impacting neuronal differentiation. Modulation of its methylation levels affects ribosome association of the fragile X mental retardation protein (FMRP) and is accompanied by an altered translation of WNT pathway-related mRNAs. Together, these data identify ribosome heterogeneity through rRNA 2′-O-me during early development and differentiation and suggest a direct role for ribosomes in regulating translation during cell fate acquisition.

## INTRODUCTION

Embryonic development requires specific and accurately dosed protein subsets with utmost spatiotemporal precision, often paralleled by profound changes in cell proliferation and overall protein synthesis rates.[1–4] In particular, the formation of the mammalian nervous system entails an exceptionally fine-tuned protein homeostasis to generate and connect hundreds of neural subtypes,[5–8] and any failure of the translation machinery derails normal brain development and function.[7,9–11] Although transcriptional, post-transcriptional, and post-translational regulations have been studied in many developmental model systems,[12–14] the role of translation, and specifically the intrinsic regulatory potential of modifications to the ribosome itself, remains understudied.[5,15]

In eukaryotes, a highly controlled and energy-consuming ribosome biosynthesis pathway ensures the correct assembly of this huge macromolecular complex made of ribosomal RNA (rRNA) and proteins (RPs).[16–18] Beyond the core ribosome, a large number of associated factors have been identified in different organisms.[19] Further complexity arises through post-translational modification of RPs and the large number of different rRNA modifications.[20] The two most abundant rRNA modifications are pseudouridines (Ψ) and 2′-O-methylations (2′-O-me).[20] Both modifications are added to specific rRNA nucleotides by generic enzymes guided by small nucleolar RNAs (snoRNAs) via complementary base-pairing interactions.

Despite the inherent complexity of the ribosome, investigation into the mechanisms by which translation is controlled has mainly focused on mRNA abundance, sequence, and secondary structure, as well as regulation by initiation and elongation factors.[21,22] However, over recent years, evidence has accumulated, suggesting that ribosomes are not generic machines but come with a considerable amount of natural and pathologic variations.[20] As such, several studies have reported variation in the RP composition through the incorporation of RP paralogs or alterations in RP stoichiometry,[23–27] and their post-translational modifications.[19] Likewise, ribosome variation can stem from changes in the rRNA post-transcriptional modification profiles.[28–31] The establishment of ribosome heterogeneity has led to the hypothesis of functional ribosome specialization, where alternating core protein composition as well as protein or rRNA

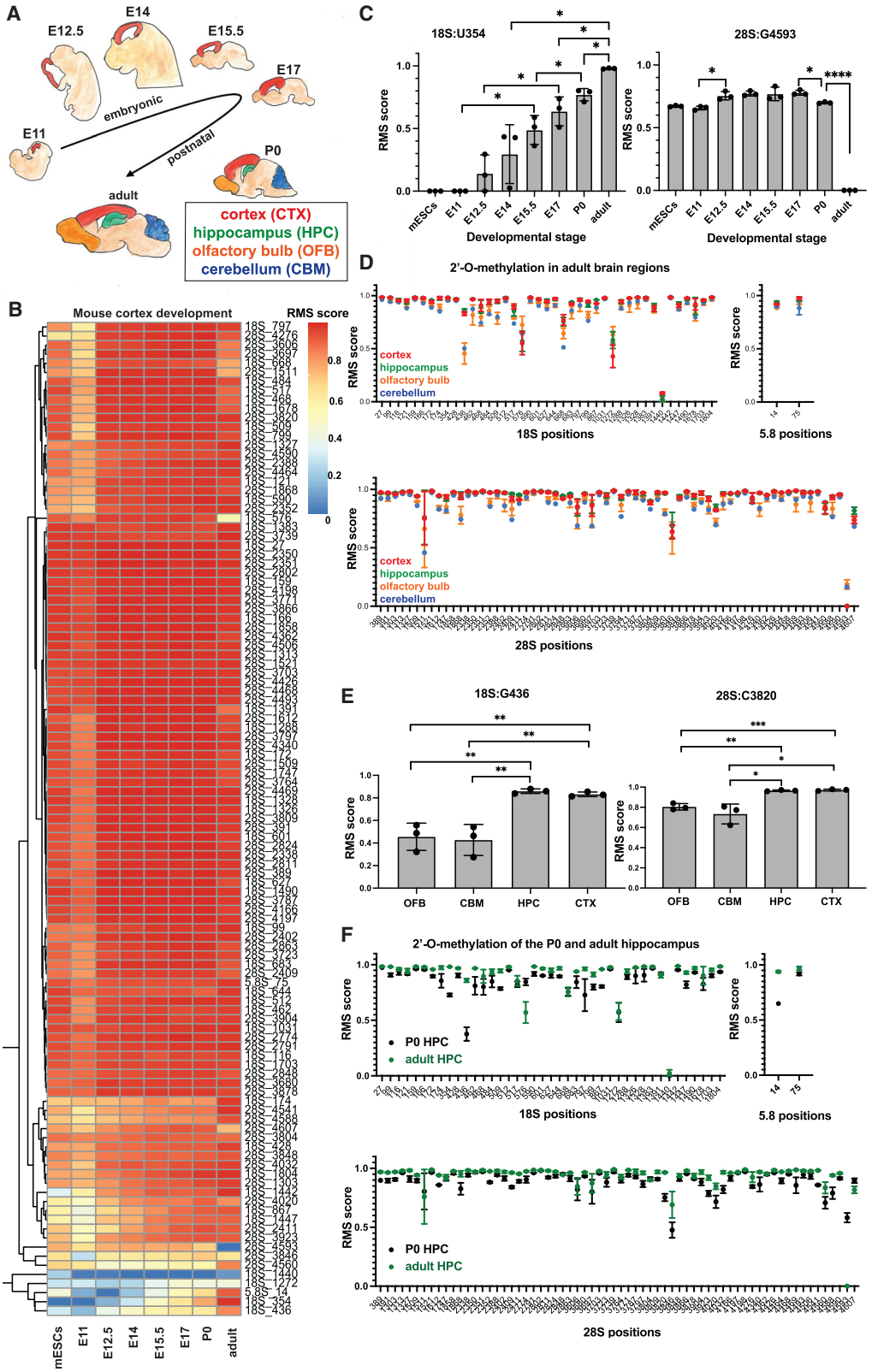


*(legend on next page)*

modifications could confer additional layers of regulation to the translation process by influencing translation speed and fidelity or promoting the translation of specific mRNA subsets.[20,28,32]

Using RiboMeth-seq (RMS),[33,34] we have previously observed that about a third of the 111 rRNA positions known to carry 2′-O-me in humans are fractionally methylated, i.e., not all ribosomes of a given cell or tissue carry a modification at one of these positions.[35,36] These findings have been corroborated by studies demonstrating variation of the rRNA 2′-O-me-profile during normal development in zebrafish and mice[37,38] and in pathologies such as diffuse large B cell lymphoma[39] and breast cancer.[40] Together, the data suggest the existence of ribosome subtypes characterized by different 2′-O-me modification patterns. Emerging experimental evidence supports the notion of 2′-O-me sites facilitating ribosome specialization. For instance, we have recently shown that expression of the MYC oncogene results in specific alterations of the ribosome 2′-O-me pattern in human cells, particularly at 18S:C174, which in turn impacts the translation of distinct mRNAs depending on their codon composition.[35]

Here, we aim to understand the importance of ribosomal 2′-O-me for cell fate establishment in early embryonic development and during neuronal specification. We show that the rRNA 2′-O-me profile undergoes significant and profound changes during mouse embryonic and postnatal brain development. Tracing development back to germ layer specification, we demonstrate that the directed differentiation of human embryonic stem cells (hESCs) into the three embryonic germ layers triggers significant differentiation type-specific 2′-O-me dynamics. The importance of these dynamics is highlighted by our finding that the removal of a single, dynamic 2′-O-me modification push cell fate toward the neurectoderm. This is mediated at least partially through an altered translation of WNT signaling pathway members and differential association of the translational regulator fragile X mental retardation protein (FMRP) in the vicinity of the modulated 2′-O-me site.

Together, these data indicate that rRNA modification constitutes a previously unrecognized and essential regulatory mechanism in regulating mammalian gene expression and establishing cellular identity.

## RESULTS

### Temporal and regional rRNA 2′-O-me dynamics during mouse brain development

Previously, we demonstrated the existence of 2′-O-me dynamics in cell culture models.[35] To investigate whether heterogeneity and dynamics of 2′-O-me exist *in vivo* during the transition from multipotent stem cells to differentiation, we focused on a developmental system with a tightly timed sequence of neurogenesis. We performed microdissection of mouse brain neocortex (CTX) during embryonic windows just prior to neurogenesis (E11), throughout neurogenesis (E12.5, E14, E15.5, and E17), and in the postnatal period after neurogenesis is complete (P0 and adult) (Figure 1A). Subsequently, RMS quantification of the 109 known 2′-O-me sites was performed on all samples in biological triplicates.

We detect pronounced changes to rRNA 2′-O-me patterns over the course of cortex development (Figure 1B). In accordance with previous observations,[35,36] sub-stoichiometric methylation is detected at a subset of sites only, and significant changes in the degree of 2′-O-me are seen at 43 sites (Table S1). Among the variable sites, most display an increase in 2′-O-me levels over the course of neocortex development. Some positions transit from undetectable to fully methylated (such as 18S:U354), whereas other sites display a late but substantial drop in methylation levels at the adult stage, for example, at 28S:G4593 (Figure 1C). We observe hypo-methylation at embryonic stage (E11) when the neuroepithelium is yet to commit to a more restricted neural stem cell lineage at E12.5, giving rise to pyramidal neurons throughout subsequent embryonic stages. The 2′-O-me profile of mouse embryonic stem cells (mESCs) cultured *in vitro* more closely resembles the multipotent E11 neuroepithelium (Figure 1B). Interestingly, most changes in the maturing neocortex are sequential and progressive over time, perhaps indicating a role for rRNA methylation dynamics in the stepwise acquisition of mature neuronal fate (Figure 1B).

We next asked whether the neocortex rRNA methylation profile is aligned with other brain regions in the postnatal period. Toward that, we additionally microdissected hippocampus (HPC), cerebellum (CBM), and olfactory bulb (OFB) tissue from the same neonates and adult animals used for the cortex development analysis and performed RMS (Figures 1D and S1A). We identified 9 positions with significant differences between at least two brain regions at the P0 stage and 8 positions in the adult (Table S1). Two examples in the adult, 18S:G436 and 28S:C3820, are shown in Figure 1E. Both positions displayed higher methylation levels in the cortex and HPC compared with the CBM and the OFB. More generally, the 2′-O-me profiles of the cortex and HPC and those of the CBM and OFB, respectively, form two separate clusters, consistent with their divergent neurodevelopmental origins (Figure S1B).

Subsequently, we extended our comparison to the 2′-O-me profiles of the same four brain regions between neonates (P0)

**Figure 1. rRNA 2′-O-me dynamics in the developing mouse brain**

(A) Murine model system. Cortex from 7 developmental stages. Hippocampus, olfactory bulb, and cerebellum from neonates (P0) and adult.

(B) rRNA 2′-O-me levels in the developing mouse cortex and a mESC line measured by RiboMeth-seq (RMS scores). Columns: developmental stages, rows: all rRNA positions known to be potentially 2′-O-methylated from the 28S, 18S, and 5.8S rRNA. Color scale (blue low, red high) indicates the mean RMS score from three biological replicates.

(C) RMS scores for two examples of rRNA sites displaying 2′-O-me dynamics during mouse cortex development, position 18S:U354 and 28S:G4593. Columns indicate mean RMS score for each condition of n = 3 sequenced libraries from different animals, points denote each value separately. Error bars represent ±SD. *p $\leq$ 0.05, **p $\leq$ 0.01, ***p $\leq$ 0.001, ****p $\leq$ 0.0001 (Welch's unpaired t test).

(D) Comparison of RMS scores between four brain regions from adult mice. Known methylated positions from the 28S, 18S, and 5.8S rRNA are depicted on separate graphs on the x axis. y axis: average RMS score. Points represent mean RMS scores of n = 3 sequenced libraries from different animals. Error bars represent ±SD.

(E) As (C), for RMS scores at 18S:G436 in different brain regions (OFB, olfactory bulb; CBM, cerebellum; HPC, hippocampus; CTX, cortex) at the adult stage.

(F) As (D), for hippocampus of neonates (P0) (black) and adult mice (green).

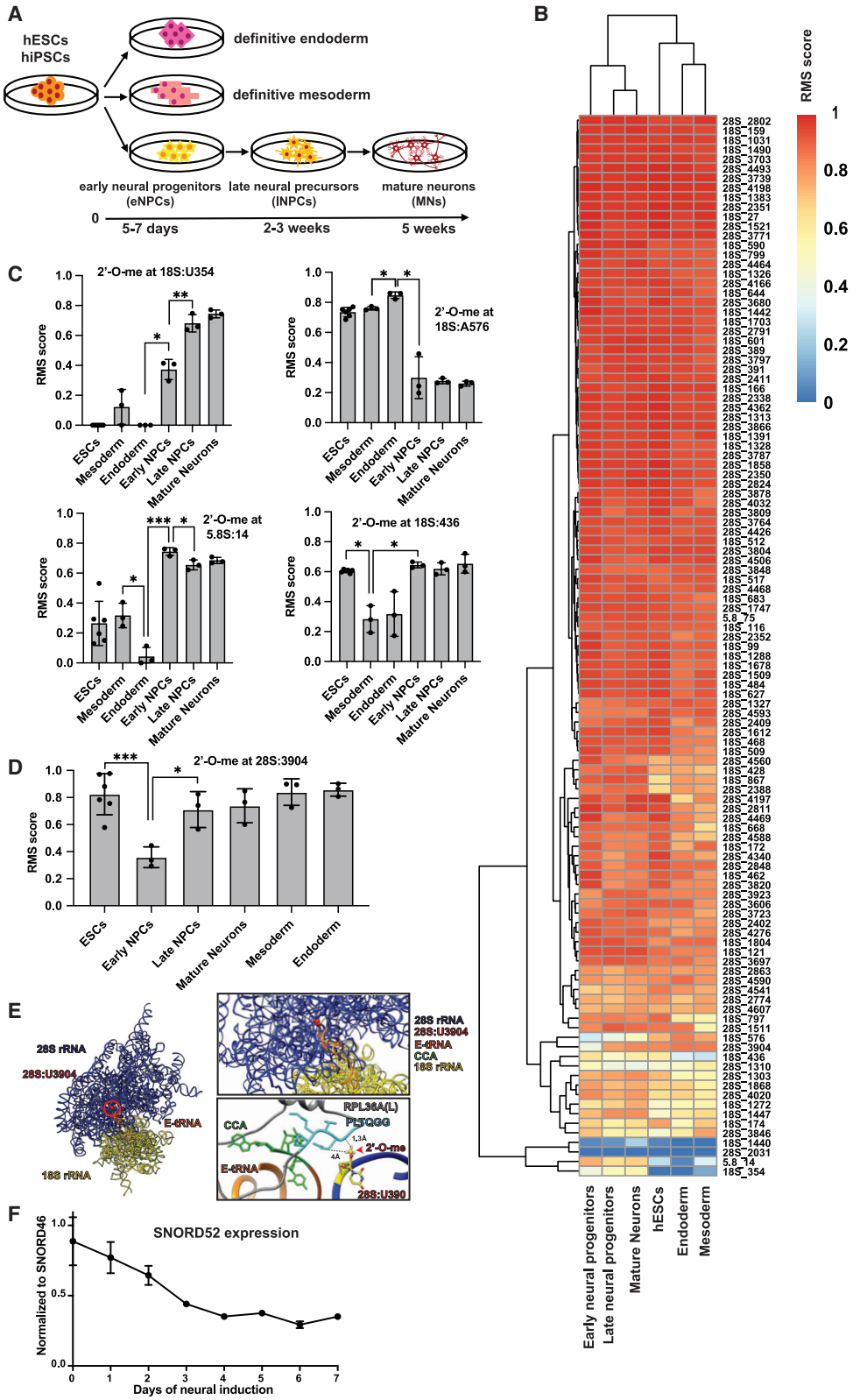


*(legend on next page)*

and adult mice, identifying further marked differences (Figures 1F and S1C; Table S1). Notably, the 2′-O-me level at 28S:G4593 drops substantially to almost zero in all brain regions only after birth (Table S1), demonstrating that dynamic changes in 2′-O-me continue to take place in the postnatal brain. Interestingly, 28S:G4593 is the only common postnatally dynamic position in all four regions, as both the number of significantly changing positions (7 in CTX, 3 in OFB, 6 in CBM, and 9 in HPC) and their combination vary between the areas (Table S1). This reinforces the idea that the acquisition of regional identity is paralleled by the establishment of a specific combination of rRNA modifications and indicates a different composition of ribosome subtypes. Importantly, the 2′-O-me RMS values display a remarkable reproducibility between replicates, although the samples come from independent animals. This suggests that the changes to rRNA 2′-O-me are tightly regulated during mouse brain development.

## Fate-specific 2′-O-me dynamics during hESC differentiation

Our identification of dynamic rRNA 2′-O-me sites within the developmental transition from multipotency to differentiation in mouse neural tissue raised the question of whether 2′-O-me dynamics occur during earlier stages of stem cell commitment. We therefore analyzed totipotent hESC differentiation into the three germ layers. For this purpose, we differentiated two hESC lines (H9 and HUES4), as well as a human induced pluripotent stem cell (iPSC) line (KOLF2) into the three embryonic germ layers: endoderm, mesoderm, and ectoderm (Figure 2A). The ectoderm differentiation, in particular, consists of a stepwise restriction of pluripotency, first giving rise to early neural progenitor cells (eNPCs), then to late neural progenitor cells (lNPCs), and finally mature neurons (MNs) (Figure 2A). Appropriate generation of the desired cell types over the course of differentiation was confirmed by reverse transcription-quantitative polymerase chain reaction (RT-qPCR) analysis for a panel of pluripotency and germ layer markers (Figures S2A and S2B) and immunohistochemistry (Figure S2C). All three cell lines differentiated as expected, with the exception of ectoderm formation, where only the H9 cell line differentiated adequately and was thus used for further experiments (Figure S2D). RMS was subsequently performed on all three cell lines in their pluripotent state and on their differentiated progeny (Figures 2B and S3A). All three pluripotent cell lines showed very similar 2′-O-me profiles at both the pluripotent and differentiated stages, indicating that the observed dynamics were robust and reproducible (Figure S3A).

Significant dynamics in 2′-O-me, at a subset of positions, were observed during the transition of stem cells into endoderm, mesoderm, and ectoderm (Figure 2B; Table S2). Strikingly, the combination of sites changing dynamically was type-specific differentiation, suggesting that different compositions of 2′-O-methylated ribosome subtypes are required for divergent differentiation processes (Figure 2C; Table S2). For instance, position 18S:A576 was nearly fully methylated in pluripotency and maintained this level upon endoderm and mesoderm differentiation, but methylation dropped significantly during ectoderm differentiation. In contrast, position 18S:U354 2′-O-me levels remained close to undetectable in all samples, except for ectoderm differentiation, where full methylation was gradually reached. As for position 18S:G436, the methylation level was stable during ectoderm differentiation compared with pluripotent cells but significantly decreased during endoderm and mesoderm generation. Finally, position 5.8S:U14 displayed a different dynamics for each type of differentiation: the 2′-O-me level remains stable in mesoderm, decreases in endoderm, and increases in ectoderm differentiation (Figure 2C). Moreover, some site-specific 2′-O-me dynamics observed *in vivo* during mouse brain development were recapitulated at the corresponding positions during human neurogenesis *in vitro*. As such, both models show a marked loss of methylation at position 18S:A576 and a substantial increase at position 18S:U354 over time (Figures 1A, 1B, and 2C).

Position 28S:U3904 sparked our interest, as it displayed intriguing 2′-O-me dynamics specifically upon neural differentiation: its methylation levels were high in hESCs and all three germ layers (RMS scores: 0.71–0.82), except for a transient drop to an RMS score of 0.36 at the eNPC stage, the earliest cell fate commitment intermediate during ectoderm differentiation, often also referred to as “neurectoderm” (Figure 2D). This observation prompted us to speculate that this transient decrease in 2′-O-me levels might be connected to, or even required for, epiblast-to-neurectoderm transition. 28S:U3904 is located in the immediate vicinity of the ribosome E site in the catalytic peptidyl transferase center and the RP RPL36A(L) (Figure 2E).

**Figure 2. 2′-O-me dynamics during directed differentiation of hESCs**

(A) Human model system. hESCs (H9, HUES4) and hiPSCs (KOLF2) were differentiated into the 3 embryonic germ layers endoderm, mesoderm, and ectoderm. Neural differentiation (ectoderm) is subdivided into early neural progenitor cells (eNPCs), late neural precursor cells (lNPCs), and mature neurons (MNs).

(B) Mean RMS scores of n = 6 sequenced libraries for $H9^{WT}$ cells at the pluripotent stage (hESCs) and n = 3 differentiated into endoderm, mesoderm, and ectoderm, respectively (columns). Ectoderm is divided into early neural progenitor cells (eNPCs), late neural progenitor cells (lNPCs), and mature neurons (MNs). Rows: all rRNA positions known to be potentially methylated from the 28S, 18S, and 5.8S rRNA. Methylation levels range from absent (RMS score = 0, blue) to full (RMS score = 1, red).

(C) Different types of rRNA 2′-O-me dynamics at the indicated positions during $H9^{WT}$ differentiation into the 3 embryonic germ layers measured by RiboMeth-seq. Cell stages are indicated on the x axis, and the y axis represents the fraction of rRNA molecules carrying a methylation at a certain position in these samples (RMS score). Error bars represent ±SD of biological replicates (n = 6 for ESCs, n = 3 for other samples). *$p \leq 0.05$, **$p \leq 0.01$, ***$p \leq 0.001$, ****$p \leq 0.0001$ (Welch’s unpaired t test).

(D) rRNA 2′-O-me dynamics at 28S:U3904 upon $H9^{WT}$ differentiation into the three embryonic germ layers measured by RiboMeth-seq (n = 6 for ESCs, n = 3 for other samples). Error bars represent ±SD. *$p \leq 0.05$, **$p \leq 0.01$, ***$p \leq 0.001$, ****$p \leq 0.0001$ (Welch’s unpaired t test).

(E) Left: localization of 28S:U3904 in the 3D structure of human rRNA. Blue: large subunit (28S). Yellow: small subunit (18S). Orange: tRNA. Red: 28S:U3904. Right, top: close up of the human ribosome region harboring 28S:U3904, color code as (left). Right, bottom: 3D configuration of 2′-O-methylated 28S:U3904 (yellow), the CCA-portion of the E-tRNA (green/orange) and the conserved PLTQGG motif of ribosomal protein RPL36A(L) (cyan/gray).

(F) SNORD52 expression during early neural induction of $H9^{WT}$, assayed by RT-qPCR and normalized to SNORD46. Points indicate mean of n = 3 biological replicates, error bars represent ±SD.

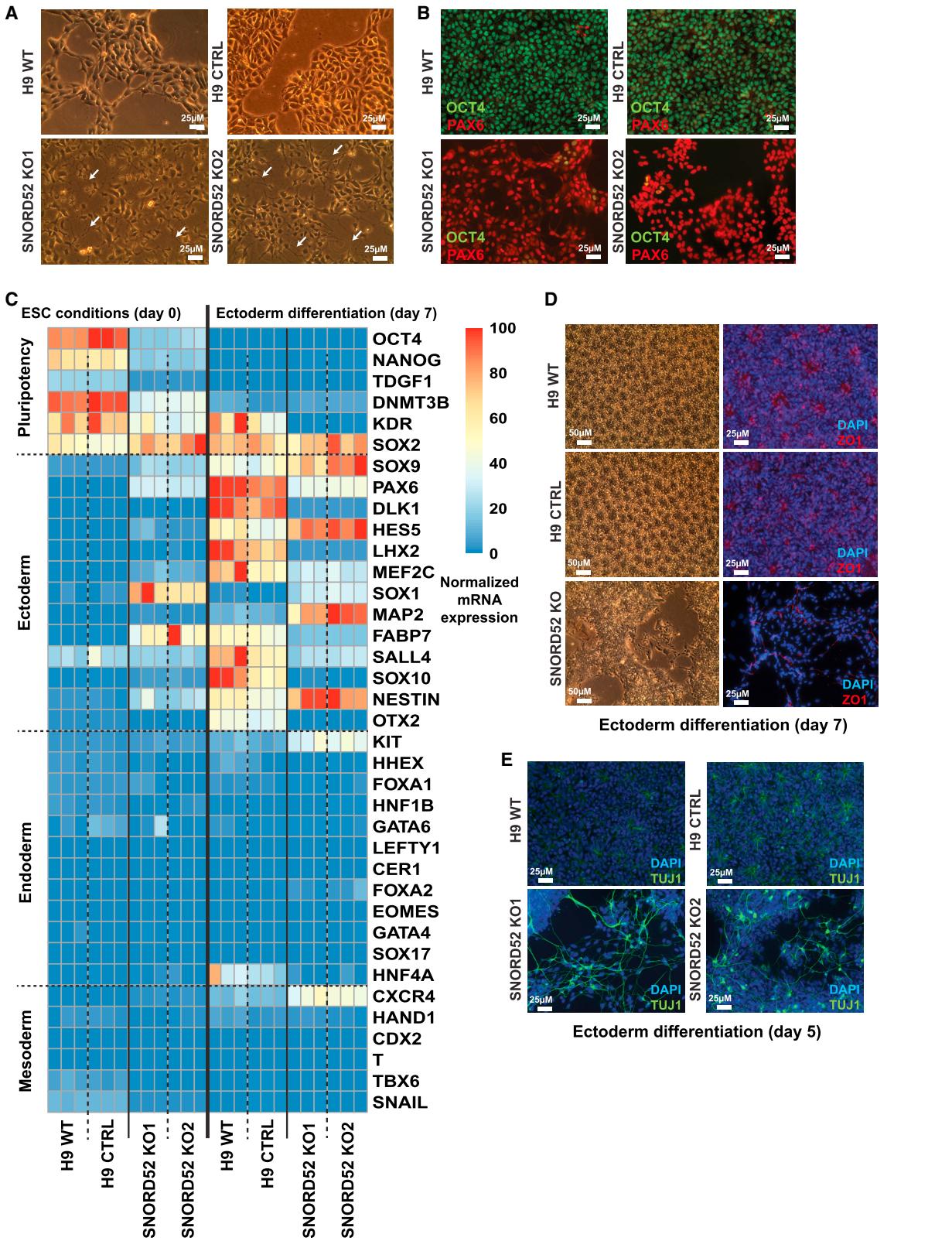


*(legend on next page)*

28S:U3904 2′-O-me is guided by SNORD52, and in line with the drop of methylation, the expression level of SNORD52 was also decreased upon neural induction, which recapitulates the epiblast-to-neurectoderm transition (in the present protocol, eNPCs emerge between days 7 and 10) (Figure 2F).

## Loss of 28S:U3904-me in hESCs shifts cell identity toward the neural fate

To investigate a potential causative link between specific 2′-O-me dynamics and cell fate in the transition from ESC to NPC in the ectoderm lineage, we manipulated the methylation levels of position 28S:U3904 by modulating the expression of the associated snoRNA guide. The genomic locus of SNORD52 locates in the third intron of a long noncoding RNA (lncRNA) of unknown function, *SNHG32* (Figure S4A). This lncRNA hosts an additional snoRNA in its first exon, SNORD48, which guides the positioning of 2′-O-me at 28S:C1868 (Figures S4A and S4B). With the striking exception of ectoderm differentiation, the 2′-O-me dynamics at these two positions were comparable (Figure S4C). In addition, *SNHG32* was expressed at very low steady-state levels in all cell types examined here, whereas SNORD48 levels are high, and SNORD52 displays moderate expression (Figure S4D), thus arguing for differential regulation of host genes and snoRNAs.

Using CRISPR-Cas9 editing (Figure S4E), we excised SNORD52 from wild-type H9 hESCs ($H9^{WT}$) and characterized two independent full knockout (KO) clones ($H9^{52KO}$) (Figures S4F and S4G). Complete loss of methylation at 28S:U3904 was confirmed by RMS (Figure S4H).

Several CRISPR-negative clones (having undergone the exact same procedure as the $H9^{52KO}$ clones but without a successful deletion) were analyzed in parallel and referred to as $H9^{CTRL}$ (Figure S4F).

Although cultured under the same stringent ESC conditions as the $H9^{WT}$ cells and the $H9^{CTRL}$ clones, the $H9^{52KO}$ clones displayed marked morphological differences compared with the former. They exhibited features characteristic of eNPCs, such as small neurite outgrowths (Figure 3A). Moreover, $H9^{52KO}$ cells displayed lower proliferation rates compared with the wild type (Figure S5A). Strikingly, although both $H9^{52KO}$ clones stained positive for the early neural transcription factor *PAX6*, the expression of the pluripotency marker *OCT4* was markedly reduced in comparison with H9 wild-type and $H9^{CTRL}$ cells (Figure 3B). Marker gene profiling by qRT-PCR of stemness and differentiation markers confirmed that the $H9^{52KO}$ clones expressed lower levels of several pluripotency marker genes, particularly *OCT4* and *NANOG*. In contrast, they displayed upregulation of a subset of ectoderm-specific markers, such as *NESTIN*, *SOX1*, and FABP7, but not of endodermal or mesodermal marker transcripts (Figure 3C, left). These findings suggest that the loss of 28S:U3904 2′-O-me shifted the cellular identity of hESCs toward a neural fate. $H9^{52KO}$ cells seem to adopt an identity of NPCs, where the levels of 28S:U3904 are naturally lowest (Figure 2D). This would also explain the slight change in RMS score seen at positions 28S:A1310 and 28S:A3846 in the $H9^{52KO}$ compared with $H9^{WT}$ (Figure S4H), given that these display a decrease and an increase in RMS score, respectively, during neurogenesis (Figure 2B).

To investigate the effect of manipulating 28S:U3904 2′-O-me levels on differentiation and cell fate decision-making, we subjected $H9^{WT}$, $H9^{CTRL}$, and $H9^{52KO}$ cells to directed differentiation into the three embryonic germ layers. Upon ectoderm differentiation, $H9^{WT}$ and $H9^{CTRL}$ cells formed a dense monolayer patterned by neural rosettes, staining positive for ZO1 (Figure 3D), typical for early forebrain progenitors.[45] In contrast, $H9^{52KO}$ cells grew less densely and did not form neural rosettes (Figure 3D) but rapidly developed neurite-like extensions and networks and strongly expressed the eNPC and INPC marker NESTIN (Figure S5B), as well as the later neural markers Tuj1 (β-tubulin III) (Figure 3E) and MAP2 (Figure S5B) well in advance compared with $H9^{WT}$.

Marker gene expression profiling illustrated that on day 7 of ectoderm induction, $H9^{WT}$, $H9^{CTRL}$, and $H9^{52KO}$ cell lines had effectively shut down pluripotency markers and selectively upregulated ectoderm-related genes (Figure 3C, right). In contrast, $H9^{52KO}$ cells displayed higher levels of *SOX1*, *NESTIN*, and *MAP2* but lower levels of *SOX10*, *PAX6*, and *DLK1*. Interestingly, the $H9^{52KO}$ cells displayed higher levels of *PAX6* at day 0, which remained relatively stable and seemed refractory to the transient upregulation of *PAX6* between days 3 and 5 as seen in $H9^{WT}$ and $H9^{CTRL}$ cells (Figure S5C). Moreover, several genes failed entirely to be upregulated in the $H9^{52KO}$ cells, including *OTX2*, *LHX2*, and *SOX10* (Figure S5C). In addition, $H9^{52KO}$ cells showed incomplete or failed endoderm and mesoderm differentiation upon induction of these two germ layers, and instead, the cells formed atypical tridimensional structures (Figure S5D). Endoderm and mesoderm markers, like *CER1* or *T/BRACHYURY*, were either absent or displayed delayed upregulation (Figures S5E and S5F). $H9^{52KO}$-derived endoderm also displayed the aberrant expression of the ectoderm marker *SOX1* (Figure S5E).

To verify that $H9^{52KO}$ cells had indeed assumed a neuroectodermal-like fate, we performed RNA-seq on $H9^{52KO}$ and $H9^{WT}$ and compared the differentially expressed genes with those in RNA-seq data from haploid H9 hESCs differentiation into the 3 embryonic germ layers.[46] We analyzed the available data for differential expression of genes occurring during each type of

**Figure 3. Loss of 2′-O-me at 28S:U3904 shifts cell identity from ESCs to NPCs under ES conditions and biases differentiation potential toward neurogenesis**

(A) Representative bright-field images of $H9^{WT}$ ESCs (WT), CRISPR control $H9^{CTRL}$ (CTRL), and two SNORD52 knockout ($H9^{52KO}$) clones (KO1 and KO2) under hESC culture conditions (n = 3). Magnification: 20×. White arrows indicate neuritic outgrowths. Scale bars indicate 25μm.

(B) Immunofluorescence staining of $H9^{WT}$, $H9^{CRTL}$, and $H9^{52KO}$ clones for the pluripotency transcription factor OCT4 (green) and the neurogenesis transcription factor PAX6 (red) under hESC culture conditions (n = 3). Magnification 20×. Scale bars indicate 25μm.

(C) Normalized RT-qPCR assay of markers for pluripotency and differentiation into the 3 germ layers (rows) applied to $H9^{WT}$, $H9^{CTRL}$, and two $H9^{52KO}$ clones as biological triplicates (columns) under hESC conditions (day 0) and at day 7 of ectoderm differentiation.

(D) Bright-field and immunofluorescence images of $H9^{WT}$, $H9^{CTRL}$, and $H9^{52KO}$ (clone 1) cells at day 7 of neural induction (n = 4). Magnification 10×. Blue: DAPI. Red: ZO1, for visualization of neural rosette structures. Scale bars indicate 25μm.

(E) Immunofluorescence staining at day 5 of neural differentiation of $H9^{WT}$, $H9^{CTRL}$, and two $H9^{52KO}$ clones using nuclear staining (DAPI, blue) and an antibody against neuron-specific TUJ1 (β-tubulin III, green) (n = 3). Magnification: 20×. Scale bars indicate 25μm.

differentiation and also defined gene sets with expression changes unique to each particular differentiation type (Figures S6A–S6C; Table S3).

The comparison of differentially expressed genes in H9$^{52KO}$ cells to those from each differentiation type showed a much stronger correlation with the neuroectodermal set than to those of mesoderm and endoderm (Figure S6D). Furthermore, when the correlation analysis was performed against the genes with differentiation type-specific expression changes, H9$^{52KO}$ cells displayed a strong positive correlation only with the neuroectodermal set, with mesodermal and endodermal distinct genes showing no or negative correlations (Figure S6E).

To ensure that the observed effect of 28S:U3904 loss was not cell line specific, we knocked out SNORD52 also in the RC17 hESC line and investigated two independent clones (Figure S7A). RC17$^{52KO}$ cells formed neurosphere-like clusters detaching from the matrigel and proliferating in suspension. As observed in the H9 line, RC17$^{52KO}$ cells exhibited downregulation of pluripotency markers under stem cell conditions, with the exception of the neural stem cell marker *SOX2*, whose expression increased alongside multiple neurogenesis-specific genes compared with RC17$^{WT}$ and RC17$^{CTRL}$ cells (Figure S7B). Subjected to differentiation into the three germ layers, the RC17$^{52KO}$ clones displayed a faster and stronger upregulation of neural genes upon ectoderm differentiation, notably at day 3, and an earlier expression of later neurogenesis markers, such as *MAP2* at day 5 (Figure S7B). Similar to the H9$^{52KO}$ cells, RC17$^{52KO}$ cells exhibited a disorganized gene expression during endoderm differentiation (Figure S7C) and failed to upregulate nearly all tested markers upon mesoderm differentiation (Figure S7D).

To assess if increased 2′-O-me levels at 28S:U3904 in hESCs would also impact cell identity, we overexpressed SNORD52 from an EGFP intron in H9$^{WT}$ and characterized two H9$^{52OE}$ clones. Stable expression of EGFP was verified at the ESC stage (Figure S8A) and upon differentiation (Figure S8B). As expected, we observed higher expression levels of SNORD52 at the ESC stage and throughout differentiation (Figure S8C), and 2′-O-me levels at position 28S:U3904 were slightly, although not significantly, increased relative to the H9$^{WT}$ under hESC conditions (Figure S8D). Despite restoring 2′-O-me levels at 28S:U3904, reintroduction of SNORD52 into the H9$^{52KO}$ cells did not revert them to the ESC stage but rather induced growth arrest and terminal neural differentiation (Figure S5G). Although the expression of germ-layer-specific markers (Figure S8E) suggests that H9$^{52OE}$ cells are competent for differentiation into all three germ layers, the cells differed from H9$^{WT}$ specifically for ectoderm differentiation. Notably, the cells did not form neural rosettes (Figure S8F). Moreover, H9$^{52OE}$ cells expressed some marker genes, such as *OTX2*, at higher levels than H9$^{WT}$, which the H9$^{52KO}$ cells failed to upregulate or express at low levels (Figure S8G).

These results indicate that abrogation of 2′-O-me at 28S:U3904 in hESCs suffices to drive the cells out of pluripotency and toward a neural cell fate and potentially modulate the neurogenic potential.

## Loss of 2′-O-me at 28S:U3904 does not impact ribosome biogenesis

Installment of certain rRNA modifications, including 2′-O-me, is required for accurate ribosome biogenesis and assembly, generally through stabilizing the local ribosome structure.[29,47,48] Northern blot analysis for the different rRNA intermediates identified no imbalance, indicative of ribosome biogenesis defect upon loss of 2′-O-me at 28S:U3904, although an overall reduction of processing intermediates was observed in both the H9$^{52KO}$ cells and H9$^{WT}$-derived eNPCs (H9$^{NPC}$) compared with the H9$^{WT}$ cells, hinting an overall reduced number of ribosomes (Figure S9A). This was confirmed by measuring the total RNA quantity obtained from equal numbers of H9$^{52KO}$ cells and H9$^{WT}$ cells (Figure S9B) and by quantifying 18S and 28S rRNA. H9$^{52KO}$ cells contained about 50% fewer ribosomes than H9$^{WT}$ without an alteration in the respective amounts of subunit rRNA (Figure S9C).

This is consistent with several studies describing significant variations in both ribosome numbers per cell and overall translation during neural differentiation.[5,6] Indeed, a peptide synthesis assessment via O-propargyl-puromycin (OPP) incorporation showed reduced global translation in H9$^{NPC}$ and H9$^{52KO}$ compared with H9$^{WT}$ cells, with the H9$^{52KO}$ levels being similar to those of the H9$^{NPC}$ (Figure S9D).

Given that both ribosome and translation levels are comparable between H9$^{NPC}$ and H9$^{52KO}$ cells, we assume that the decrease in ribosome numbers that we observe in the H9$^{52KO}$ cells is rather a consequence of the shift toward the neural fate than the result of a biogenesis defect, which fits previously reported observations.[49]

## 28S:U3904 2′-O-me levels influence long-term neural cell identity

Following on from the clear bias toward neuroectoderm differentiation observed in H9$^{52KO}$ cells, we proceeded to further characterize the neurogenic potential of H9$^{52KO}$ cells by differentiating the cells into MNs, alongside H9$^{WT}$ and H9$^{52OE}$-derived NPCs (H9$^{52OE\text{-}NPC}$). Neural maturation was allowed for 50 days and was expected to produce primarily forebrain-type neurons and glia.[45] In addition to morphology monitoring, the expression of a broad panel of brain region-specific markers was assessed by RT-qPCR at several time points. 2 weeks into the maturation phase, the H9$^{52KO}$ cells consistently developed a distinct morphological phenotype compared with the H9$^{WT}$ and H9$^{52OE}$ cells. Although H9$^{WT}$ and H9$^{52OE}$ cells formed a homogeneous neural network, the H9$^{52KO}$ cells grew first into a dense monolayer and then formed multiple circular cavities rimmed by thick borders with cilia-like cell protuberances (Figure 4A). Gene expression analysis at the early neural induction phase (days 3 and 7) showed suppression of forebrain-associated genes (*LHX2*, *FEZF1*, *FOXG1*, *SIX3*, and *OTX1/2*) and concomitant induction of hindbrain genes (*HOXA2*, *HOXB1*, and *IRX3*) in the H9$^{52KO}$ cells compared with the H9$^{WT}$ cells (Figure 4B).[50]

In addition, terminal maturation of the cultures further identified the emergence of *TTR*+/*OTX2*+/*MAP2*− (Figure 4C) choroid plexus cells additionally expressing *AQP1* and *GDF7* (Figure 4B) in the H9$^{52KO}$ but not the H9$^{WT}$ cultures.

H9$^{52OE}$ cells in turn displayed an expression pattern similar to the one of H9$^{WT}$ cells during early differentiation time points; however, the expression levels of forebrain genes were attenuated compared with H9$^{WT}$ and the cells upregulated di/mesencephalon markers (*BARHL1* and *LMX1A*) at day 7. At the mature stage, H9$^{52OE}$ cells assumed a more posterior signature

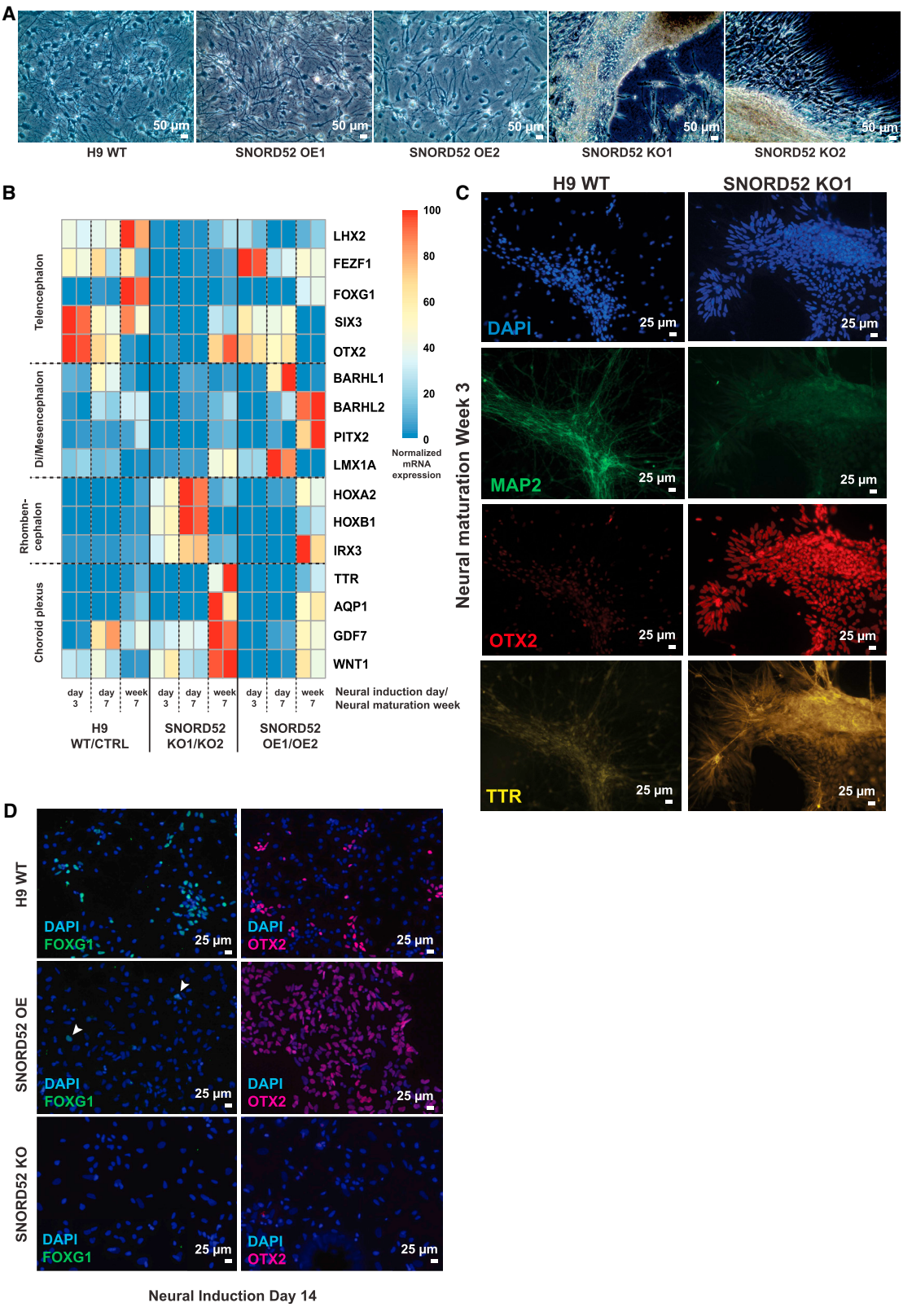


*(legend on next page)*

(*BARHL2*, *PITX2*, *FOXA2*, and *WNT1*) (Figure 4B). Moreover, the gradient of *FOXG1* and *OTX2* staining intensity from $H9^{WT}$ (strong) over $H9^{52OE}$ (intermediate) to $H9^{52KO}$ cells (absent) at the eNPC stage further supports a di/rhombencephalic shift of $H9^{52OE}$ and $H9^{52KO}$ cells (Figure 4D).

Altogether, these data indicate that the perturbation of 2′-O-me at 28S:3904 at the stem cell stage could impact on the regional identity of the derived MNs (Figure 4D).

## 2′-O-me at 28S:U3904 influences translation of mRNAs involved in the WNT pathway

To investigate whether the methylation status of 28S:U3904 might influence the translation of specific mRNAs and thus explain the early shift in cell identity in SNORD52 mutants, we performed ribosome profiling of $H9^{WT}$ and $H9^{52KO}$ cells under ESC culture conditions (Figures S10A–S10I; Table S4). Detected transcripts were categorized depending on their differential regulation in $H9^{52KO}$ cells into those with significant differences in mRNA expression (transcription only), ribosome occupancy (translation only), and both transcription and translation, opposite changes, or no change. The majority of changes (6,615 transcripts) fell into the class of concordant changes in transcription and translation (Figure 5A). Fitting previous observations, most transcriptionally upregulated genes in the $H9^{52KO}$ cells were related to neural cell identity or function (Figure S10H), thus confirming once more that the $H9^{52KO}$ cells indeed shifted toward neuroectoderm. Moreover, the top categories of transcriptionally downregulated genes are related to ribosome biogenesis, thus matching our observation of a reduced number of ribosomes in the $H9^{52KO}$ cells (Figure S10I). Interestingly, a subset of transcripts (1,509) was significantly changed at the level of translation only (Figure 5A; Table S4). 708 transcripts displayed decreased translation (TL-DN) in the $H9^{52KO}$ cells, and gene ontology (GO) analysis identified that these transcripts related primarily to translation and ribosome biogenesis, including RPs (Figure S10G). 801 transcripts were translationally upregulated (TL-UP) in the $H9^{52KO}$ cells, and the most enriched and only statistically significant GO category corresponded to genes related to the WNT signaling pathway (Figure 5B). The WNT/β-catenin pathway plays a complex role in pluripotency and lineage commitment, sometimes taking on opposite functions depending on the spatiotemporal context.[51] On one hand, WNT signaling is required for the induction and maintenance of stemness,[51] whereas on the other hand, differentiation comes with the release of β-catenin from the cellular membrane[52] and a surge of WNT transcriptional activity,[52,53] which notably is required for neural induction[54,55] and rostro-caudal neural tube patterning.[50,56]

Given the complexity of the pathway and the multiple layers of interaction and feedback loops between its components, it is not surprising that we find both activators and inhibitors among the WNT-related genes TL-UP in the $H9^{52KO}$ cells (Table S4).

We assessed canonical WNT activity using the TOP/FOP luciferase reporter assay.[57] In line with the findings above, WNT activity was markedly higher in the $H9^{52KO}$ cells compared with the $H9^{WT}$ and $H9^{52OE}$ under hESC conditions (Figure 5C). Moreover, upon a neural induction time course, the induction of WNT activity was markedly lower in the $H9^{52OE}$ cells compared with the $H9^{WT}$ (Figure 5D). Release of β-catenin from the cell membrane and its translocation to the cytoplasm and nucleus is an additional indicator of canonical WNT pathway activation.[52,53] For this reason, we stained $H9^{WT}$, $H9^{52KO}$, and $H9^{52OE}$ cells under ESC culture conditions for β-catenin. Levels were higher, and β-catenin localization was significantly more cytoplasmic and nuclear in the $H9^{52KO}$ cells compared with the two other cell lines, where the staining was mainly detected at the cell membrane and was lowest in the $H9^{52OE}$ cells (Figures 5E and 5F). Western blotting furthermore confirmed the translational upregulation of WNT target genes in $H9^{52KO}$ found by ribosome profiling, such as *RECK* and *CITED1* (Figure 5G).

To investigate if activation of the WNT pathway per se could explain the observed shift in cell identity, we blocked the WNT inhibitor glycogen synthase kinase 3 (GSK3) in H9 and RC17 hESCs. Inhibition of GSK3 (GSK3i) quickly reduced the expression of pluripotency genes and induced the upregulation of neurogenesis-related genes in both cell lines at mRNA (Figure S11A) and protein level (Figure S11B), but no induction of endoderm or mesoderm gene expression (Figure S11A). Interestingly, neural genes that displayed a reduced expression or no induction upon GSK3i treatment such as *OTX2*, *DLK1*, or *LHX2* (Figure S11A) also showed a decreased expression in $H9^{52KO}$ cells during early neural induction (Figure 3C), thus suggesting that GSK3i application partially phenocopies the effect of SNORD52 KO.

Hence, these data support the notion that the methylation status of 28S:U3904 impacts the capacity of the ribosome population for translating specific mRNAs.

## Ribosomes lacking 2′-O-me at 28S:U3904 display increased FMRP binding

To identify potential differences in proteins associated with the ribosomes in $H9^{WT}$, $H9^{52KO}$, and $H9^{NPC}$ cells, we purified ribosomes from the 80S (monosome) and polysome fractions from each cell type and analyzed them by mass spectrometry (Table S5). To examine proteins most likely to be truly associated with the ribosome and remove the majority of contaminants present throughout the sucrose gradients, the detected proteins were filtered using a list of ribosome-interacting proteins derived from a previous study of two human cell lines[19] (Table S5). Overall, more proteins were found significantly associated with

**Figure 4. Manipulation of 28S:U3904 2′-O-me levels modifies the long-term neural differentiation potential of hESCs**

(A) Representative bright-field images of $H9^{WT}$, $H9^{52KO}$, and $H9^{52OE}$ cells (n = 4) at day 21 of neural maturation. Magnification: 20×. Scale bars indicate 50μm.

(B) Normalized expression of brain regional markers in $H9^{WT}$, $H9^{52KO}$, and $H9^{52OE}$ cells at days 3 and 7 of early neural induction and after 7 weeks of neural maturation measured by RT-qPCR.

(C) Representative staining of $H9^{WT}$ and $H9^{52KO}$ cells (n = 3) after 3 weeks of neural maturation. Magnification: 20×. Blue: DAPI, green: MAP2, red: OTX2, yellow: TTR. Scale bars indicate 25μm.

(D) Representative staining of $H9^{WT}$, $H9^{52KO}$, and $H9^{52OE}$ cells (n = 2) at the eNPC stage. Magnification: 20×. Blue: DAPI, green: FOXG1, red: OTX2. Scale bars indicate 25μm.

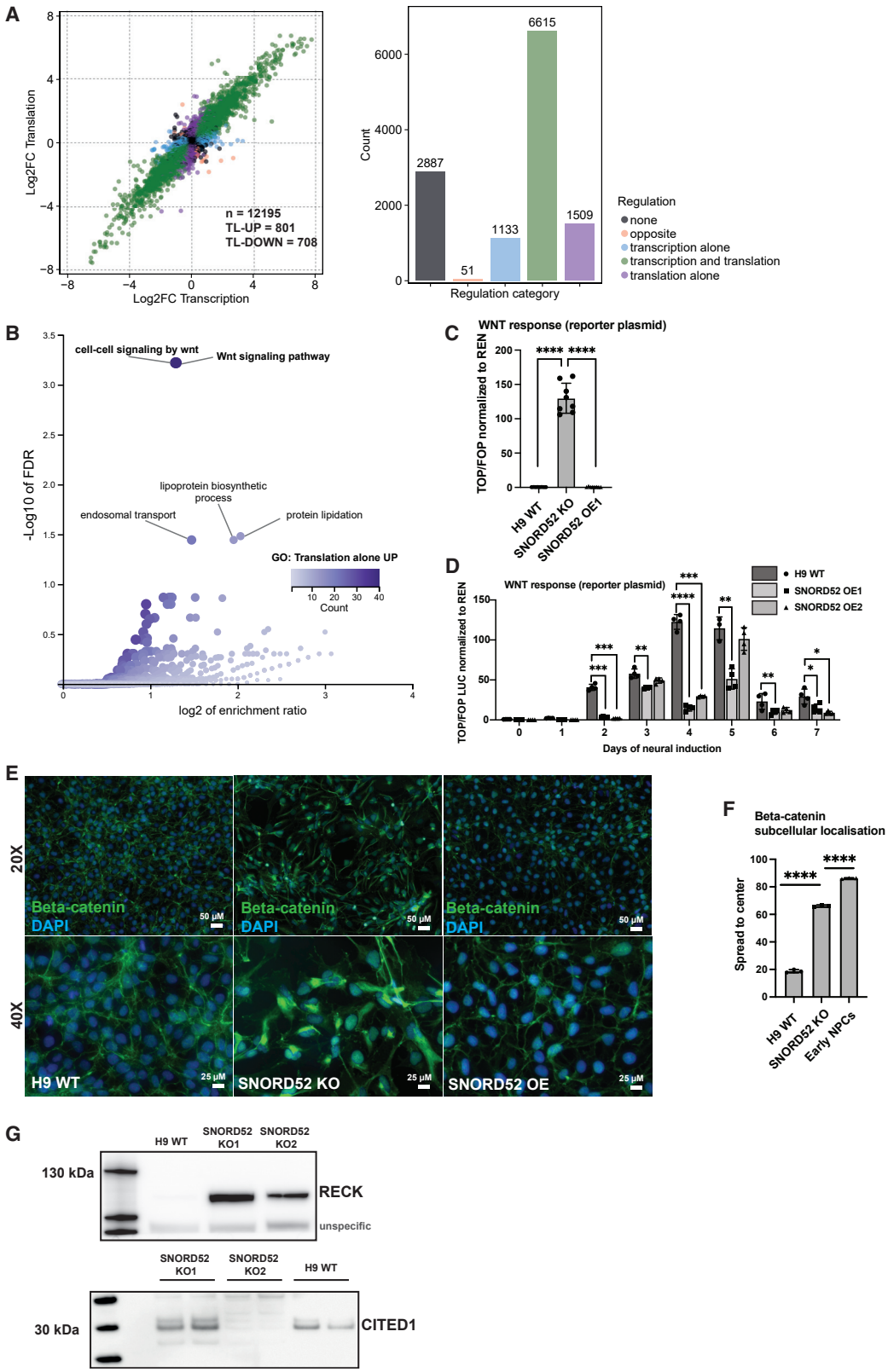


**Figure 5. WNT pathway translation is repressed by 28S:U3904 methylation**

(A) Changes in mRNA expression (transcription) and ribosome footprint levels (translation) from ribosome profiling data, comparing $H9^{WT}$ and $H9^{52KO}$ cells (n = 3 libraries from individual cultures). Scatter plot (left) with mRNA transcripts colored by indicated regulation type. Number of sequenced transcripts analyzed given

*(legend continued on next page)*

ribosomes from $H9^{WT}$ compared with either $H9^{52KO}$ or $H9^{NPC}$ cells (Figures 6A and 6B). We focused on proteins enriched in samples from $H9^{52KO}$ and $H9^{NPC}$ cells compared with $H9^{WT}$. Among these, we found FMRP to be significantly more associated with ribosomes in $H9^{52KO}$ (Figure 6A), and $H9^{NPC}$ (Figure 6C), in both 80S and polysome fractions. Moreover, FMRP is also enriched in $H9^{52KO}$ compared with $H9^{NPC}$ in the 80S fraction (Figure 6B). Despite having been shown to act at many levels of gene expression,[58] FMRP is best known for regulating translation of mRNAs involved in neurodevelopment,[59] leading to a crucial role in the regulation of the proliferation and cell fate of neural stem cells.[60] FMRP can bind both to mRNA and to the ribosome, where it is assumed to bind within the intersubunit space and hamper the binding of tRNA and translation elongation factors.[41,58,61] Cryo-EM structural analysis from *Drosophila* locates FMRP in close vicinity of 28S:U3904[41] (Figure 6E).

We confirmed the increased binding of FMRP to ribosomes devoid of 2′-O-me at 28S:U3904 by purifying ribosomes from $H9^{WT}$, $H9^{52KO}$, $H9^{52OE}$, and $H9^{NPC}$ cells through sucrose cushions and probed for FMRP binding by western blot (Figures 6D and S12). FMRP enrichment in the ribosome fraction was quantified as the ratio of ribosome-bound FMRP over total FMRP levels in the cell (input). We observe a strong enrichment of FMRP in the ribosome fraction of $H9^{52KO}$ cells compared with all other cell lines (Figures 6D, 6E, and S12).

## DISCUSSION

Over the last years, solid evidence has documented considerable ribosome heterogeneity in many organisms, and recent studies have reported on ribosome specialization supporting translation of select mRNA populations, thus indicating a more profound role for the ribosome, or ribosome subtypes, in instigating specific translation programs.[20,21,35]

This study significantly corroborates the contribution of rRNA 2′-O-me variation to ribosome diversity and provides conceptual insight into the role of differential 2′-O-me in defining early stages of development and cell fate decision-making during neurogenesis. We demonstrate profound rRNA 2′-O-me pattern differences between brain regions, which supports the hypothesis that ribosome diversification could contribute to the establishment of tissue identity. Tracking back to the early stages of development, we demonstrate that the directed differentiation of hESCs into the three germ layers is paralleled by significant, robust, and germ-layer-specific alterations to the 2′-O-me patterns of the ribosome population, suggesting a role for ribosome specialization in early development and cell fate decision-making.

Having established that rRNA 2′-O-me patterns consistently change during brain development and cell identity acquisition, we further demonstrated functionality by linking a single 2′-O-me position to a specific differentiation process and cell fate. Removal of the 2′-O-me at 28S:U3904 facilitates hESCs transition into neuroectoderm, despite being cultured under restrictive stemness conditions and compromising their ability to differentiate into the two other germ layers. Furthermore, this influences the neurogenic potential of the cells by changing their regional identity upon long-term maturation toward a more posterior nature. The fact that the reintroduction of SNORD52 into the $H9^{52KO}$ cells did not rescue the ESC phenotype is to be expected, given that the return to pluripotency, or "reprogramming," is a complicated, low-efficiency process.[62] In addition, as 28S:U3904 2′-O-me increases again when NPCs differentiate into neural precursors and MNs, it is conceivable that expressing SNORD52, in an NPC-like context, rather promotes further progress down the neural cell fate than a return to the pluripotent state.

Using ribosome profiling, we identified a set of transcripts differing only at their level of translation following ablation of 2′-O-me at 28S:U3904. GO analysis strongly indicated a role for the canonical WNT pathway, and validation experiments confirmed active WNT signaling in the $H9^{52KO}$ cells. The WNT pathway plays complex and multifaceted roles in cell identity.[51] De-repression or activation of WNT signaling either by inhibition of GSK3β[50,63] or activation of β-catenin signaling[55] facilitates the neural differentiation of hESCs. Furthermore, WNT participates in rostro-caudal organization of the neural tube, axon guidance, and synapse development and activity.[54] Regulation of WNT pathway members at the level of translation was functionally confirmed by the observation that $H9^{52KO}$ cells display strongly upregulated WNT signaling, assume an NPC-like identity at the levels of morphology, gene expression, and differentiation potential, and finally are biased toward a hindbrain final cell fate, fitting the WNT gradient-governed pattern of the neural tube.[50]

An ongoing debate in the field relates to whether ribosome heterogeneity results in ribosome specialization.[64,65] An alternative to the ribosome specialization hypothesis proposes that varying the concentration of ribosomes selectively impacts different classes of mRNAs differently, without invoking

by n. Numbers of transcripts upregulated or downregulated in $H9^{52KO}$ relative to $H9^{WT}$ cells in the translation alone set also shown (TL-UP, TL-DN, respectively). Histogram (right) giving the number of mRNA transcripts significantly regulated in each category (Benjamini-Hochberg padj < 0.05).

(B) Gene ontology analysis of mRNA transcripts in TL-UP set. Biological process GO categories with FDR < 0.05 are labeled. Number of genes overlapping with each GO category indicated by the color-scale gradient.

(C) WNT activity measured by TOP/FOP reporter assay in $H9^{WT}$ and $H9^{52}$KO cells. Luciferase activity is used as readout for WNT activity and normalized to Renilla activity from a control plasmid. The TOP plasmid contains WNT response elements, the FOP plasmid mutated versions of the latter. Columns indicate mean luciferase ratios of n = 3 independent experiments at each time point, points denote each value separately. Error bars represent ±SD. *p ≤ 0.05, **p ≤ 0.01, ***p ≤ 0.001, ****p ≤ 0.0001 (Welch's unpaired t test).

(D) The same TOP/FOP reporter assay as in (C) with $H9^{WT}$ and two $H9^{52OE}$ clones over the course of the first 7 days of neural induction. Average of n = 3 independent experiments. Error bars represent ±SD. *p ≤ 0.05, **p ≤ 0.01, ***p ≤ 0.001, ****p ≤ 0.0001 (Welch's unpaired t test).

(E) Immunofluorescence images of $H9^{WT}$, $H9^{52KO}$, and $H9^{52OE}$ cells for β-catenin (green) and nuclear staining (DAPI, blue) (n = 3). Top row magnification: 20×. Bottom row magnification: 40×. Scale bars indicate 25μm.

(F) Quantification of the subcellular localization of β-catenin in $H9^{WT}$, $H9^{52KO}$, and early neural progenitor cells derived from $H9^{WT}$ ($H9^{NPC}$). Error bars represent ±SD. ****p ≤ 0.0001 (Welch's unpaired t test).

(G) Western blot for RECK (left) and CITED1 (right) in $H9^{WT}$ and $H9^{52KO}$ cells under hESC conditions.

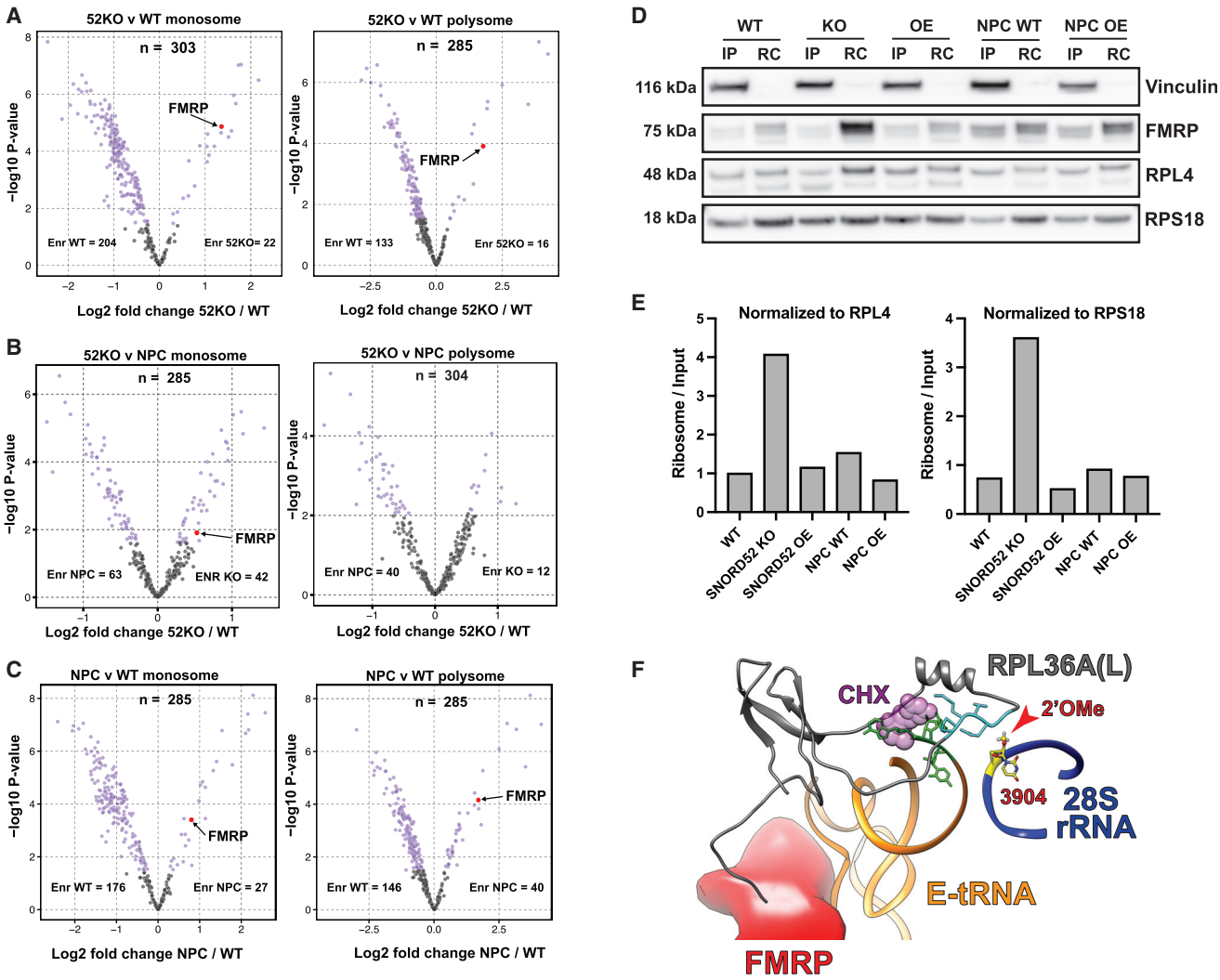


**Figure 6. FMRP preferentially binds ribosomes lacking 28S:U3904 methylation**

(A) Protein abundance changes in $H9^{52KO}$ (52KO) compared with $H9^{WT}$ (WT) ribosome-associated proteins in monosomes (left) and polysomes (right). $Log_2$-fold change in abundance (52KO/WT) and $-log_{10}$ p values shown (n = 3 independent protein samples per condition). Those significantly changing (Benjamini-Hochberg padj < 0.05) are colored (magenta). n denotes number of proteins analyzed. Numbers of proteins enriched in either sample is indicated (Enr WT, Enr 52KO). FMRP is highlighted in red.

(B) Protein abundance changes in $H9^{52KO}$ (52KO) compared with $H9^{NPC}$ (NPC) ribosome-associated proteins in monosomes (left) and polysomes (right). $Log_2$-fold change in abundance (52KO/WT) and $-log_{10}$ p values shown (n = 3 independent protein samples per condition). Those significantly changing (Benjamini-Hochberg padj < 0.05) are colored (magenta). n denotes number of proteins analyzed. Numbers of proteins enriched in either sample are indicated (Enr WT, Enr 52KO). FMRP is highlighted in red.

(C) Protein abundance changes in $H9^{NPC}$ (NPC) compared with $H9^{WT}$ (WT) ribosome-associated proteins in monosomes (left) and polysomes (right). $Log_2$-fold change in abundance (NPC/WT) and $-log_{10}$ p values shown (n = 3 independent protein samples per condition). Those significantly changing (Benjamini-Hochberg padj < 0.05) are colored (magenta). n denotes number of proteins analyzed. Numbers of proteins enriched in either sample is indicated (Enr NPC, Enr WT). FMRP is highlighted in red.

(D) Detection of total cellular and ribosome-bound FMRP protein by western blot in $H9^{WT}$ (WT), $H9^{52KO}$ (KO), $H9^{52OE}$ (OE), $H9^{NPC}$ (NPC WT), and $H9^{52OE}$-derived (NPC OE) cells. IP (input) = whole cell lysate, RC (ribosome cushion) = ribosomes purified by sucrose cushion. Vinculin serves as a control for ribosome purification. RPL4 and RPS18 levels are used to control for ribosome abundance. A representative blot out of n = 4 experiments is shown, the other blots can be seen in Figure S11.

(E) Quantification of the enrichment of FMRP in the ribosome-bound fraction based on (C). Bands were quantified, then subsequently the values for FMRP normalized to the corresponding ribosomal protein (RPL4 or RPS18), and finally, the ratio of the ribosome-bound fraction over the input fraction calculated. See Figure S9 for three more experimental repeats.

(F) 3D model of FMRP localization in the imminent vicinity of 28S:U3904, based on cryo-EM data from *Drosophila*.[41] FMRP (red) is in direct contact with the E-site tRNA (orange) and the ribosomal protein RPL36A(L) (gray), which in turn lies within contact distance of 28S:U3904 (yellow, 28S rRNA in blue). The binding position of cycloheximide (CHX, violet) is additionally shown.

specialized ribosome functions—the ribosome concentration hypothesis[1,65] In contrast, other studies have demonstrated a specialized translation program resulting from, for instance, modulation of the RP constituents[26] or rRNA modification patterns in the absence of changes to the ribosome concentration.[35,66] The two views are not necessarily contradictory, and it is conceivable that some cases are regulated by a combination of specialized ribosomes and ribosome numbers. In this study, loss of 2′-O-me at 28S:U3904 is accompanied by a drop in ribosome number in the $H9^{52KO}$ cells. As such, we cannot fully rule out that part of the observed shift in cellular identity in our system is caused by a reduction in ribosome numbers during the transition from the ESC to the neuroectoderm state. Given that this reduction to similar levels is equally observed during the differentiation of WT ESCs to NPCs, it is likely that the phenomenon is rather another feature of the neural cell fate commitment than its triggering event. Similarly, we cannot fully rule out the existence of non-ribosomal targets for SNORD52,[67] although the direct impact of 28S:U3904 loss on translation and the increased association of FMRP with $H9^{52KO}$ ribosomes renders the scenario less likely.

To gain mechanistic insight into how 2′-O-me at 28S:U3904 can modulate translation, we purified ribosomes from $H9^{WT}$, $H9^{52KO}$, and $H9^{WT}$-derived neuroectoderm and analyzed their composition using mass spectrometry. This and subsequent validations identified an increased binding of FMRP to ribosomes purified from $H9^{52KO}$ and neuroectoderm derived from $H9^{WT}$ cells. FMRP is a brain-enriched RNA-binding protein with a multitude of roles related to translation, mRNA transport, splicing, and RNA stability.[58,68] Importantly, FMRP is also implicated in neurogenesis and neural cell fate,[59,60] and loss of FMRP leads to fragile X syndrome.[69] FMRP is generally considered a translational inhibitor and has been linked to the activation of WNT signaling through the translational repression of WNT inhibitors[60,70] but recently also through the stabilization of mRNAs belonging to key WNT pathway molecules, notably *CTNNB1*.[71] Structural modeling predicts no direct interaction between FMRP and the 28S:U3904 rRNA residue. Nonetheless, both FMRP and 28S:U3904 contact the E-site tRNA and the eukaryote-specific RP RPL36AL.[72] Given that the 28S:U3904 is located less than 5 Å proximity of the methylated PLTQGG motif of RPL36A(L), this could point toward an intricate interplay of both rRNA and RP heterogeneity through a methylation hotspot with direct effects on E-tRNA stability and FMRP binding.

Altogether, our findings reinforce the idea that the ribosome itself is a direct regulator of translation and demonstrates that modulation of the ribosome through alterations in the rRNA 2′-O-me modification pattern contributes to directed differentiation and cell fate decision-making during early development.

### Limitations of the study

Both bulk RMS and RNA-seq do not account for the possible diversity of 2′-O-me profiles and transcriptomes found in the different neural cell types present *in vivo* and *in vitro*, which would require single-cell resolution (currently not possible for RMS). Moreover, *in vitro* neural differentiation of hESCs is limited in its representativeness for early brain development. Further investigation would be required to determine the connection between 28S:U3904 methylation and Wnt activation as well as the role of the various WNT pathway members, and the potential implication of other signaling routes.

## STAR★METHODS

Detailed methods are provided in the online version of this paper and include the following:

- KEY RESOURCES TABLE
- RESOURCE AVAILABILITY
  - Lead contact
  - Materials availability
  - Data and code availability
- EXPERIMENTAL MODEL AND STUDY PARTICIPANT DETAILS
  - Animals
  - Cell lines
- METHOD DETAILS
  - Cell culture
  - RNA isolation from mouse brains
  - RiboMeth-Seq
  - RiboMeth-seq Data treatment
  - Generation of loss and gain of function mutants
  - Gene expression
- 3D MODELLING
  - Ribosome profiling
  - Global nascent peptide synthesis assay
  - TOP/FOP Wnt reporter assay
  - Northern blotting analysis of rRNA processing
  - Mass spectrometry on 80S and polysomes
  - MS data acquisition
  - TMT Quantitative Proteomics Analysis
  - Proteomic mass spectrometry data analysis
- QUANTIFICATION AND STATISTICAL ANALYSIS

## SUPPLEMENTAL INFORMATION

Supplemental information can be found online at https://doi.org/10.1016/j.devcel.2023.06.007.

## ACKNOWLEDGMENTS

The Lund lab is supported by grants from the Danish Council for Independent Research (Sapere Aude program 418 3-00179B and [0169-00073B]); the Novo Nordisk Foundation (NNF21CC0073729 and NNF 0071919); the Lundbeck Foundation (R198-2015-174); and the Danish Cancer Society (R204-A12532). Furthermore, this project has received funding from the European Union's Horizon 2020 research and innovation program under the Marie Skłodowska-Curie grant agreement n° 801481 and The VILLUM Experiment Programme under the grant n° 17544. The authors would like to thank Bettina Mentz, Anna Fossum, and Elin Josefina Pietras for their technical help. Mass spectrometry analyses were performed by the Proteomics Research Infrastructure (PRI) at the University of Copenhagen (UCPH), supported by the Novo Nordisk Foundation (NNF) (grant agreement number NNF19SA0059305).

## AUTHOR CONTRIBUTIONS

S.J.H. designed most experiments, collected data, and drafted the article. M.D.J. carried out ribosome profiling, data analysis, interpretation, and mass spectrometry data analysis. K.A. performed bioinformatics data analysis. M.L.K. provided mouse brain samples and insight into brain development and ribosome structure. K.L.A. carried out mass spectrometry data collection.

CellPress

Z.A.-N and A.K. assisted with qPCR data collection and data interpretation. M.F. and D.M.S. were involved in establishing cell lines. P.M. designed and made the CRISPR-Cas9-related constructs. D.M.G., F.S.A., and D.T. provided critical input on the manuscript. N.K. contributed ribosome biogenesis-related experiments. H.N. and A.K. provided advice on data interpretation. A.H.L. and M.D.J. assisted with work conception, data interpretation, and drafting of the manuscript. All authors commented on the manuscript.

## DECLARATION OF INTERESTS

The authors declare no competing interests.

## INCLUSION AND DIVERSITY

We support inclusive, diverse, and equitable conduct of research.

Received: September 6, 2022
Revised: February 16, 2023
Accepted: June 26, 2023
Published: July 19, 2023

## REFERENCES

1. Khajuria, R.K., Munschauer, M., Ulirsch, J.C., Fiorini, C., Ludwig, L.S., McFarland, S.K., Abdulhay, N.J., Specht, H., Keshishian, H., Mani, D.R., et al. (2018). Ribosome levels selectively regulate translation and lineage commitment in human hematopoiesis. Cell *173*, 90–103.e19. https://doi.org/10.1016/j.cell.2018.02.036.
2. Kraushar, M.L., Viljetic, B., Wijeratne, H.R.S., Thompson, K., Jiao, X., Pike, J.W., Medvedeva, V., Groszer, M., Kiledjian, M., Hart, R.P., et al. (2015). Thalamic WNT3 secretion spatiotemporally regulates the neocortical ribosome signature and mRNA translation to specify neocortical cell subtypes. J. Neurosci. *35*, 10911–10926. https://doi.org/10.1523/JNEUROSCI.0601-15.2015.
3. Magee, J.A., and Signer, R.A.J. (2021). Developmental stage-specific changes in protein synthesis differentially sensitize hematopoietic stem cells and erythroid progenitors to impaired ribosome biogenesis. Stem Cell Rep. *16*, 20–28. https://doi.org/10.1016/j.stemcr.2020.11.017.
4. Wang, R., and Amoyel, M. (2022). mRNA translation is dynamically regulated to instruct stem cell fate. Front. Mol. Biosci. *9*, 863885. https://doi.org/10.3389/fmolb.2022.863885.
5. Baser, A., Skabkin, M., Kleber, S., Dang, Y., Gülcüler Balta, G.S., Kalamakis, G., Göpferich, M., Ibañez, D.C., Schefzik, R., Lopez, A.S., et al. (2019). Onset of differentiation is post-transcriptionally controlled in adult neural stem cells. Nature *566*, 100–104. https://doi.org/10.1038/s41586-019-0888-x.
6. Blair, J.D., Hockemeyer, D., Doudna, J.A., Bateup, H.S., and Floor, S.N. (2017). Widespread translational remodeling during human neuronal differentiation. Cell Rep. *21*, 2005–2016. https://doi.org/10.1016/j.celrep.2017.10.095.
7. Kapur, M., Monaghan, C.E., and Ackerman, S.L. (2017). Regulation of mRNA translation in neurons—A matter of life and death. Neuron *96*, 616–637. https://doi.org/10.1016/j.neuron.2017.09.057.
8. Kraushar, M.L., Krupp, F., Harnett, D., Turko, P., Ambrozkiewicz, M.C., Sprink, T., Imami, K., Günnigmann, M., Zinnall, U., Vieira-Vieira, C.H., et al. (2021). Protein synthesis in the developing neocortex at near-atomic resolution reveals Ebp1-mediated neuronal proteostasis at the 60S tunnel exit. Mol. Cell *81*, 304–322.e16. https://doi.org/10.1016/j.molcel.2020.11.037.
9. Laguesse, S., Creppe, C., Nedialkova, D.D., Prévot, P.-P., Borgs, L., Huysseune, S., Franco, B., Duysens, G., Krusy, N., Lee, G., et al. (2015). A dynamic unfolded protein response contributes to the control of cortical neurogenesis. Dev. Cell *35*, 553–567. https://doi.org/10.1016/j.devcel.2015.11.005.
10. Lauria, F., Bernabò, P., Tebaldi, T., Groen, E.J.N., Perenthaler, E., Maniscalco, F., Rossi, A., Donzel, D., Clamer, M., Marchioretto, M., et al. (2020). SMN-primed ribosomes modulate the translation of transcripts related to spinal muscular atrophy. Nat. Cell Biol. *22*, 1239–1251. https://doi.org/10.1038/s41556-020-00577-7.
11. Yamada, S.B., Gendron, T.F., Niccoli, T., Genuth, N.R., Grosely, R., Shi, Y., Glaria, I., Kramer, N.J., Nakayama, L., Fang, S., et al. (2019). RPS25 is required for efficient RAN translation of C9orf72 and other neurodegenerative disease-associated nucleotide repeats. Nat. Neurosci. *22*, 1383–1388. https://doi.org/10.1038/s41593-019-0455-7.
12. Mohammed, H., Hernando-Herraez, I., Savino, A., Scialdone, A., Macaulay, I., Mulas, C., Chandra, T., Voet, T., Dean, W., Nichols, J., et al. (2017). Single-cell landscape of transcriptional heterogeneity and cell fate decisions during mouse early gastrulation. Cell Rep. *20*, 1215–1228. https://doi.org/10.1016/j.celrep.2017.07.009.
13. Wang, Y.-C., Peterson, S.E., and Loring, J.F. (2014). Protein post-translational modifications and regulation of pluripotency in human stem cells. Cell Res. *24*, 143–160. https://doi.org/10.1038/cr.2013.151.
14. Zhao, B.S., Roundtree, I.A., and He, C. (2017). Post-transcriptional gene regulation by mRNA modifications. Nat. Rev. Mol. Cell Biol. *18*, 31–42. https://doi.org/10.1038/nrm.2016.132.
15. Lins, É.M., Oliveira, N.C.M., Reis, O., Ferrasa, A., Herai, R., Muotri, A.R., Massirer, K.B., and Bengtson, M.H. (2022). Genome-wide translation control analysis of developing human neurons. Mol. Brain *15*, 55. https://doi.org/10.1186/s13041-022-00940-9.
16. Baßler, J., and Hurt, E. (2019). Eukaryotic ribosome assembly. Annu. Rev. Biochem. *88*, 281–306. https://doi.org/10.1146/annurev-biochem-013118-110817.
17. Khatter, H., Myasnikov, A.G., Natchiar, S.K., and Klaholz, B.P. (2015). Structure of the human 80S ribosome. Nature *520*, 640–645. https://doi.org/10.1038/nature14427.
18. Ramakrishnan, V. (2002). Ribosome structure and the mechanism of translation. Cell *108*, 557–572. https://doi.org/10.1016/S0092-8674(02)00619-0.
19. Imami, K., Milek, M., Bogdanow, B., Yasuda, T., Kastelic, N., Zauber, H., Ishihama, Y., Landthaler, M., and Selbach, M. (2018). Phosphorylation of the ribosomal protein RPL12/uL11 affects translation during mitosis. Mol. Cell *72*, 84–98.e9. https://doi.org/10.1016/j.molcel.2018.08.019.
20. Gay, D.M., Lund, A.H., and Jansson, M.D. (2022). Translational control through ribosome heterogeneity and functional specialization. Trends Biochem. Sci. *47*, 66–81. https://doi.org/10.1016/j.tibs.2021.07.001.
21. Genuth, N.R., and Barna, M. (2018). The discovery of ribosome heterogeneity and its implications for gene regulation and organismal life. Mol. Cell *71*, 364–374. https://doi.org/10.1016/j.molcel.2018.07.018.
22. Sternberg, S.H., Fei, J., Prywes, N., McGrath, K.A., and Gonzalez, R.L. (2009). Translation factors direct intrinsic ribosome dynamics during translation termination and ribosome recycling. Nat. Struct. Mol. Biol. *16*, 861–868. https://doi.org/10.1038/nsmb.1622.
23. Fusco, C.M., Desch, K., Dörrbaum, A.R., Wang, M., Staab, A., Chan, I.C.W., Vail, E., Villeri, V., Langer, J.D., and Schuman, E.M. (2021). Neuronal ribosomes exhibit dynamic and context-dependent exchange of ribosomal proteins. Nat. Commun. *12*, 6127. https://doi.org/10.1038/s41467-021-26365-x.
24. Gupta, V., and Warner, J.R. (2014). Ribosome-omics of the human ribosome. RNA *20*, 1004–1013. https://doi.org/10.1261/rna.043653.113.
25. Kondrashov, N., Pusic, A., Stumpf, C.R., Shimizu, K., Hsieh, A.C., Ishijima, J., Shiroishi, T., and Barna, M. (2011). Ribosome-mediated specificity in hox mRNA translation and vertebrate tissue patterning. Cell *145*, 383–397. https://doi.org/10.1016/j.cell.2011.03.028.
26. Shi, Z., Fujii, K., Kovary, K.M., Genuth, N.R., Röst, H.L., Teruel, M.N., and Barna, M. (2017). Heterogeneous ribosomes preferentially translate distinct subpools of mRNAs genome-wide. Mol. Cell *67*, 71–83.e7. https://doi.org/10.1016/j.molcel.2017.05.021.
27. Slavov, N., Semrau, S., Airoldi, E., Budnik, B., and van Oudenaarden, A. (2015). Differential stoichiometry among core ribosomal proteins. Cell Rep. *13*, 865–873. https://doi.org/10.1016/j.celrep.2015.09.056.

28. Shi, Z., and Barna, M. (2015). Translating the genome in time and space: specialized ribosomes, RNA regulons, and RNA-binding proteins. Annu. Rev. Cell Dev. Biol. *31*, 31–54. https://doi.org/10.1146/annurev-cellbio-100814-125346.

29. Sloan, K.E., Warda, A.S., Sharma, S., Entian, K.-D., Lafontaine, D.L.J., and Bohnsack, M.T. (2017). Tuning the ribosome: the influence of rRNA modification on eukaryotic ribosome biogenesis and function. RNA Biol. *14*, 1138–1152. https://doi.org/10.1080/15476286.2016.1259781.

30. Xue, S., and Barna, M. (2012). Specialized ribosomes: a new frontier in gene regulation and organismal biology. Nat. Rev. Mol. Cell Biol. *13*, 355–369. https://doi.org/10.1038/nrm3359.

31. Rajan, K.S., Zhu, Y., Adler, K., Doniger, T., Cohen-Chalamish, S., Srivastava, A., Shalev-Benami, M., Matzov, D., Unger, R., Tschudi, C., et al. (2020). The large repertoire of 2′-O-methylation guided by C/D snoRNAs on Trypanosoma brucei rRNA. RNA Biol. *17*, 1018–1039. https://doi.org/10.1080/15476286.2020.1750842.

32. Norris, K., Hopes, T., and Aspden, J.L. (2021). Ribosome heterogeneity and specialization in development. Wiley Interdiscip. Rev. RNA *12*, e1644. https://doi.org/10.1002/wrna.1644.

33. Birkedal, U., Christensen-Dalsgaard, M., Krogh, N., Sabarinathan, R., Gorodkin, J., and Nielsen, H. (2015). Profiling of ribose methylations in RNA by high-throughput sequencing. Angew. Chem. *127*, 461–465. https://doi.org/10.1002/ange.201408362.

34. Krogh, N., Birkedal, U., and Nielsen, H. (2017). RiboMeth-seq: profiling of 2′-O-Me in RNA. In RNA Methylation Methods in Molecular Biology, A. Lusser, ed. (Springer), pp. 189–209. https://doi.org/10.1007/978-1-4939-6807-7_13.

35. Jansson, M.D., Häfner, S.J., Altinel, K., Tehler, D., Krogh, N., Jakobsen, E., Andersen, J.V., Andersen, K.L., Schoof, E.M., Ménard, P., et al. (2021). Regulation of translation by site-specific ribosomal RNA methylation. Nat. Struct. Mol. Biol. *28*, 889–899. https://doi.org/10.1038/s41594-021-00669-4.

36. Krogh, N., Jansson, M.D., Häfner, S.J., Tehler, D., Birkedal, U., Christensen-Dalsgaard, M., Lund, A.H., and Nielsen, H. (2016). Profiling of 2′- *O* -Me in human rRNA reveals a subset of fractionally modified positions and provides evidence for ribosome heterogeneity. Nucleic Acids Res. *44*, 7884–7895. https://doi.org/10.1093/nar/gkw482.

37. Hebras, J., Krogh, N., Marty, V., Nielsen, H., and Cavaillé, J. (2020). Developmental changes of rRNA ribose methylations in the mouse. RNA Biol. *17*, 150–164. https://doi.org/10.1080/15476286.2019.1670598.

38. Ramachandran, S., Krogh, N., Jørgensen, T.E., Johansen, S.D., Nielsen, H., and Babiak, I. (2020). The shift from early to late types of ribosomes in zebrafish development involves changes at a subset of rRNA 2′- *O* -Me sites. RNA *26*, 1919–1934. https://doi.org/10.1261/rna.076760.120.

39. Krogh, N., Asmar, F., Côme, C., Munch-Petersen, H.F., Grønbæk, K., and Nielsen, H. (2020). Profiling of ribose methylations in ribosomal RNA from diffuse large B-cell lymphoma patients for evaluation of ribosomes as drug targets. NAR Cancer *2*, zcaa035. https://doi.org/10.1093/narcan/zcaa035.

40. Marcel, V., Kielbassa, J., Marchand, V., Natchiar, K.S., Paraqindes, H., Nguyen Van Long, F., Ayadi, L., Bourguignon-Igel, V., Lo Monaco, P., Monchiet, D., et al. (2020). Ribosomal RNA 2′O-methylation as a novel layer of inter-tumour heterogeneity in breast cancer. NAR Cancer *2*, zcaa036. https://doi.org/10.1093/narcan/zcaa036.

41. Chen, E., Sharma, M.R., Shi, X., Agrawal, R.K., and Joseph, S. (2014). Fragile X mental retardation protein regulates translation by binding directly to the ribosome. Mol. Cell *54*, 407–417. https://doi.org/10.1016/j.molcel.2014.03.023.

42. Bertero, A., Pawlowski, M., Ortmann, D., Snijders, K., Yiangou, L., Cardoso De Brito, M., Brown, S., Bernard, W.G., Cooper, J.D., Giacomelli, E., et al. (2016). Optimized inducible shRNA and CRISPR/Cas9 platforms for *in vitro* studies of human development using hPSCs. Development *143*, 4405–4418. https://doi.org/10.1242/dev.138081.

43. Ernlund, A.W., Schneider, R.J., and Ruggles, K.V. (2018). RIVET: comprehensive graphic user interface for analysis and exploration of genome-wide translatomics data. BMC Genomics *19*, 809. https://doi.org/10.1186/s12864-018-5166-z.

44. Liao, Y., Wang, J., Jaehnig, E.J., Shi, Z., and Zhang, B. (2019). WebGestalt 2019: gene set analysis toolkit with revamped UIs and APIs. Nucleic Acids Res. *47*. W199–W205. https://doi.org/10.1093/nar/gkz401.

45. Pankratz, M.T., Li, X.-J., LaVaute, T.M., Lyons, E.A., Chen, X., and Zhang, S.-C. (2007). Directed neural differentiation of human embryonic stem cells via an obligated primitive anterior stage. Stem Cells *25*, 1511–1520. https://doi.org/10.1634/stemcells.2006-0707.

46. Yilmaz, A., Braverman-Gross, C., Bialer-Tsypin, A., Peretz, M., and Benvenisty, N. (2020). Mapping gene circuits essential for germ layer differentiation via loss-of-function screens in haploid human embryonic stem cells. Cell Stem Cell *27*, 679–691.e6. https://doi.org/10.1016/j.stem.2020.06.023.

47. Liang, X.H., Liu, Q., and Fournier, M.J. (2007). rRNA modifications in an intersubunit bridge of the ribosome strongly affect both ribosome biogenesis and activity. Mol. Cell *28*, 965–977. https://doi.org/10.1016/j.molcel.2007.10.012.

48. Polikanov, Y.S., Melnikov, S.V., Söll, D., and Steitz, T.A. (2015). Structural insights into the role of rRNA modifications in protein synthesis and ribosome assembly. Nat. Struct. Mol. Biol. *22*, 342–344. https://doi.org/10.1038/nsmb.2992.

49. Chau, K.F., Shannon, M.L., Fame, R.M., Fonseca, E., Mullan, H., Johnson, M.B., Sendamarai, A.K., Springel, M.W., Laurent, B., and Lehtinen, M.K. (2018). Downregulation of ribosome biogenesis during early forebrain development. eLife *7*, e36998. https://doi.org/10.7554/eLife.36998.

50. Rifes, P., Isaksson, M., Rathore, G.S., Aldrin-Kirk, P., Møller, O.K., Barzaghi, G., Lee, J., Egerod, K.L., Rausch, D.M., Parmar, M., et al. (2020). Modeling neural tube development by differentiation of human embryonic stem cells in a microfluidic WNT gradient. Nat. Biotechnol. *38*, 1265–1273. https://doi.org/10.1038/s41587-020-0525-0.

51. De Jaime-Soguero, A., Abreu De Oliveira, W.A., and Lluis, F. (2018). The pleiotropic effects of the canonical Wnt pathway in early development and pluripotency. Genes *9*, 93. https://doi.org/10.3390/genes9020093.

52. Sierra, R.A., Hoverter, N.P., Ramirez, R.N., Vuong, L.M., Mortazavi, A., Merrill, B.J., Waterman, M.L., and Donovan, P.J. (2018). *TCF7L1* suppresses primitive streak gene expression to support human embryonic stem cell pluripotency. Development *145*, 161075. https://doi.org/10.1242/dev.161075.

53. Faunes, F., Hayward, P., Descalzo, S.M., Chatterjee, S.S., Balayo, T., Trott, J., Christoforou, A., Ferrer-Vaquer, A., Hadjantonakis, A.-K., Dasgupta, R., et al. (2013). A membrane-associated β-catenin/Oct4 complex correlates with ground-state pluripotency in mouse embryonic stem cells. Development *140*, 1171–1183. https://doi.org/10.1242/dev.085654.

54. Mulligan, K.A., and Cheyette, B.N.R. (2012). Wnt signaling in vertebrate neural development and function. J. Neuroimmune Pharmacol. *7*, 774–787. https://doi.org/10.1007/s11481-012-9404-x.

55. Otero, J.J., Fu, W., Kan, L., Cuadra, A.E., and Kessler, J.A. (2004). β-catenin signaling is required for neural differentiation of embryonic stem cells. Development *131*, 3545–3557. https://doi.org/10.1242/dev.01218.

56. Fang, Z., Liu, X., Wen, J., Tang, F., Zhou, Y., Jing, N., and Jin, Y. (2019). SOX21 ensures rostral forebrain identity by suppression of WNT8B during neural regionalization of human embryonic stem cells. Stem Cell Rep. *13*, 1038–1052. https://doi.org/10.1016/j.stemcr.2019.10.013.

57. Barolo, S. (2006). Transgenic Wnt/TCF pathway reporters: all you need is Lef? Oncogene *25*, 7505–7511. https://doi.org/10.1038/sj.onc.1210057.

58. Richter, J.D., and Zhao, X. (2021). The molecular biology of FMRP: new insights into fragile X syndrome. Nat. Rev. Neurosci. *22*, 209–222. https://doi.org/10.1038/s41583-021-00432-0.

59. Li, M., Shin, J., Risgaard, R.D., Parries, M.J., Wang, J., Chasman, D., Liu, S., Roy, S., Bhattacharyya, A., and Zhao, X. (2020). Identification of FMR1-regulated molecular networks in human neurodevelopment. Genome Res. *30*, 361–374. https://doi.org/10.1101/gr.251405.119.

60. Luo, Y., Shan, G., Guo, W., Smrt, R.D., Johnson, E.B., Li, X., Pfeiffer, R.L., Szulwach, K.E., Duan, R., Barkho, B.Z., et al. (2010). Fragile X mental retardation protein regulates proliferation and differentiation of adult neural stem/progenitor cells. PLoS Genet. *6*, e1000898. https://doi.org/10.1371/journal.pgen.1000898.

61. Khandjian, E.W., Corbin, F., Woerly, S., and Rousseau, F. (1996). The fragile X mental retardation protein is associated with ribosomes. Nat. Genet. *12*, 91–93. https://doi.org/10.1038/ng0196-91.

62. Takahashi, K., Tanabe, K., Ohnuki, M., Narita, M., Ichisaka, T., Tomoda, K., and Yamanaka, S. (2007). Induction of pluripotent stem cells from adult human fibroblasts by defined factors. Cell *131*, 861–872. https://doi.org/10.1016/j.cell.2007.11.019.

63. Shimojo, D., Onodera, K., Doi-Torii, Y., Ishihara, Y., Hattori, C., Miwa, Y., Tanaka, S., Okada, R., Ohyama, M., Shoji, M., et al. (2015). Rapid, efficient, and simple motor neuron differentiation from human pluripotent stem cells. Mol. Brain *8*, 79. https://doi.org/10.1186/s13041-015-0172-4.

64. Ferretti, M.B., and Karbstein, K. (2019). Does functional specialization of ribosomes really exist? RNA *25*, 521–538. https://doi.org/10.1261/rna.069823.118.

65. Mills, E.W., and Green, R. (2017). Ribosomopathies: there's strength in numbers. Science *358*, eaan2755. https://doi.org/10.1126/science.aan2755.

66. McMahon, M., Contreras, A., Holm, M., Uechi, T., Forester, C.M., Pang, X., Jackson, C., Calvert, M.E., Chen, B., Quigley, D.A., et al. (2019). A single H/ACA small nucleolar RNA mediates tumor suppression downstream of oncogenic RAS. eLife *8*, e48847. https://doi.org/10.7554/eLife.48847.

67. Falaleeva, M., and Stamm, S. (2013). Processing of snoRNAs as a new source of regulatory non-coding RNAs: SnoRNA fragments form a new class of functional RNAs. BioEssays *35*, 46–54. https://doi.org/10.1002/bies.201200117.

68. Hale, C.R., Sawicka, K., Mora, K., Fak, J.J., Kang, J.J., Cutrim, P., Cialowicz, K., Carroll, T.S., and Darnell, R.B. (2021). FMRP regulates mRNAs encoding distinct functions in the cell body and dendrites of CA1 pyramidal neurons. eLife *10*, e71892. https://doi.org/10.7554/eLife.71892.

69. Santoro, M.R., Bray, S.M., and Warren, S.T. (2012). Molecular mechanisms of fragile X syndrome: A twenty-year perspective. Annu. Rev. Pathol. *7*, 219–245. https://doi.org/10.1146/annurev-pathol-011811-132457.

70. Casingal, C.R., Kikkawa, T., Inada, H., Sasaki, Y., and Osumi, N. (2020). Identification of FMRP target mRNAs in the developmental brain: FMRP might coordinate Ras/MAPK, Wnt/β-catenin, and mTOR signaling during corticogenesis. Mol. Brain *13*, 167. https://doi.org/10.1186/s13041-020-00706-1.

71. Pedini, G., Buccarelli, M., Bianchi, F., Pacini, L., Cencelli, G., D'Alessandris, Q.G., Martini, M., Giannetti, S., Sasso, F., Melocchi, V., et al. (2022). FMRP modulates the Wnt signalling pathway in glioblastoma. Cell Death Dis. *13*, 719. https://doi.org/10.1038/s41419-022-05019-w.

72. Hountondji, C., Bulygin, K., Créchet, J.-B., Woisard, A., Tuffery, P., Nakayama, J., Frolova, L., Nierhaus, K.H., Karpova, G., and Baouz, S. (2014). The CCA-end of P-tRNA contacts both the human RPL36AL and the A-site bound translation termination factor eRF1 at the peptidyl transferase center of the Human 80S ribosome. Open Biochem. J. *8*, 52–67. https://doi.org/10.2174/1874091X01408010052.

73. Jansson, M.D., Damas, N.D., Lees, M., Jacobsen, A., and Lund, A.H. (2015). miR-339-5p regulates the p53 tumor-suppressor pathway by targeting MDM2. Oncogene *34*, 1908–1918. https://doi.org/10.1038/onc.2014.130.

74. Ingolia, N.T., Lareau, L.F., and Weissman, J.S. (2011). Ribosome profiling of mouse embryonic stem cells reveals the complexity and dynamics of mammalian proteomes. Cell *147*, 789–802. https://doi.org/10.1016/j.cell.2011.10.002.

## STAR★METHODS

### KEY RESOURCES TABLE

| REAGENT or RESOURCE | SOURCE | IDENTIFIER |
|---|---|---|
| **Antibodies** | | |
| Mouse monoclonal anti-OCT4 | Stem Cell Technologies | Cat# 60093; RRID: AB_2801346 |
| Rabbit polyclonal anti- PAX6 | Stem Cell Technologies | Cat# 60094 |
| Mouse monoclonal anti- ZO1 | BD Biosciences | Cat# 610966; RRID: AB_398279 |
| Mouse monoclonal anti-TUJ1 | Stem Cell Technologies | Cat# 60092 |
| Mouse monoclonal anti- MAP2 | Abcam | Cat# ab28032; RRID: AB_776173 |
| Mouse monoclonal anti-NESTIN | Stem Cell Technologies | Cat# 60091; RRID: AB_2905494 |
| Rabbit polyclonal anti-OTX2 | Abcam | Cat# ab2808-1; RRID: AB_2157168 |
| Sheep polyclonal anti-TTR | Bio-Rad | Cat# AHP1837; RRID: AB_2212089 |
| Goat polyclonal anti-SOX17 | R&D Systems | Cat# AF1924; RRID: AB_355060 |
| Goat polyclonal anti-T/BRACHYURY | R&D Systems | Cat# AF2085; RRID: AB_2200235 |
| Rabbit polyclonal anti-Beta Catenin | Cell Signaling Technologies | Cat# 9587; RRID: AB_10695312 |
| Rabbit polyclonal anti- FOXG1 | Abcam | Cat# ab18259; RRID: AB_732415 |
| Rabbit monoclonal anti-RECK | Cell Signalling Technologies | Cat# 3433; RRID: AB_2238311 |
| Mouse monoclonal anti-CITED1 | Merck | Cat# 424M-1 |
| Mouse monoclonal anti-Vinculin | Sigma Aldrich | Cat# V9131; RRID: AB_477629 |
| Rabbit polyclonal anti-FMRP | Cell Signaling Technologies | Cat# 4317; RRID: AB_1903978 |
| Mouse monoclonal anti-RPL4 | Santa Cruz Biotechnology | Cat# sc-100838; RRID: AB_2181910 |
| Rabbit polyclonal anti-RPS18 | LSBio | Cat# LS-C162774 |
| Goat anti-Mouse IgG (H+L) Highly Cross-Adsorbed Secondary Antibody, Alexa Fluor 488 | Thermo Fisher Scientific | Cat# A-11029; RRID: AB_2534088 |
| Goat anti-Mouse IgG (H+L) Highly Cross-Adsorbed Secondary Antibody, Alexa Fluor 594 | Thermo Fisher Scientific | Cat# A-11032; RRID: AB_2534091 |
| Donkey anti-Goat IgG (H+L) Cross-Adsorbed Secondary Antibody, Alexa Fluor™ 594 | Thermo Fisher Scientific | Cat# A-11058; RRID: AB_2534105 |
| Donkey Anti-Sheep IgG H&L (Alexa Fluor® 594) | Abcam | Cat# ab150180; RRID: AB_2716768 |
| Goat anti-Rabbit IgG (H+L) Highly Cross-Adsorbed Secondary Antibody, Alexa Fluor 488 | Thermo Fisher Scientific | Cat# A-11034; RRID: AB_2576217 |
| Donkey anti-Rabbit IgG (H+L) Highly Cross-Adsorbed Secondary Antibody, Alexa Fluor 594 | Thermo Fisher Scientific | Cat# A-21207; RRID: AB_141637 |
| **Biological samples** | | |
| Mouse brain cortex stages E11, E12.5, E14, E15.5, E17, P0, adult from CD1 mice | Charité – Universitätsmedizin Berlin | N/A |
| Mouse hippocampus P0, adult, CD1 mice | Charité – Universitätsmedizin Berlin | N/A |
| Mouse olfactory bulb P0, adult, CD1 mice | Charité – Universitätsmedizin Berlin | N/A |
| Mouse cerebellum P0, adult, CD1 mice | Charité – Universitätsmedizin Berlin | N/A |
| **Chemicals, peptides, and recombinant proteins** | | |
| Y-27632 (dihydrochloride) Rock Inhibitor | LC laboratories | Cat# Y-5301 |
| CHIR99201 GSK3 inhibitor | Axon Medchem | Cat# 1386 |
| Poly-L-ornithine | Sigma Aldrich | Cat# P3655 |
| Laminin | Sigma Aldrich | Cat# L2020 |

(*Continued on next page*)

*Continued*

| REAGENT or RESOURCE | SOURCE | IDENTIFIER |
|---|---|---|
| Cycloheximide | Sigma Aldrich | Cat# C4859 |
| **Critical commercial assays** | | |
| STEMDiff Trilineage Differentiation Kit | Stem Cell Technologies | Cat# 05230 |
| STEMdiff Forebrain Neuron Differentiation Kit | Stem Cell Technologies | Cat# 08600 |
| STEMdiff Forebrain Neuron Maturation Kit | Stem Cell Technologies | Cat# 08605 |
| mTESR Plus | Stem Cell Technologies | Cat# 100-0276 |
| TeSR-E8 | Stem Cell Technologies | Cat# 05990 |
| STEMdiuff Neural Progenitor Medium | Stem Cell Technologies | Cat# 05833 |
| hESC-qualified Matrigel | Corning | Cat# 354277 |
| Neural Progenitor Freezing medium | Stem Cell Technologies | Cat# 05838 |
| Click-iT Plus OPP Protein Synthesis Assay Kit | Life Technologies | Cat# C10457<br>Cat# C10456 |
| TruSeq Ribo Profile Mammalian Library Prep Kit | Illumina | Cat# RPYSC12116,<br>Cat# RPHMR12126 |
| Ion PI™ Hi-Q™ OT2 200 Kit | Life Technologies | Cat# A26434 |
| Ion PI™ Hi-Q™ Sequencing 200 Kit | Life Technologies | Cat# A26433 |
| Ion PI Chip Kit v.3 | Life Technologies | Cat# A26770 |
| P3 Primary Cell 4D-Nucleofector X kit | Lonza | Cat# V4XP-3024 |
| Lipofectamine 3000 Transfection reagent | Thermo Fisher | Cat# L3000001 |
| Mirus2020 transfection reagent | MirusBio | Cat# MIR5404 |
| Dual-Glo Luciferase Assay System | Promega | Cat# E2920 |
| TaqManReverese Transcription Kit | Applied Biosystems | Cat# N80803234 |
| Fast SYBR Green Master Mix | Thermo Fisher Scientific | Cat# 4385612 |
| **Deposited data** | | |
| RMS raw and analyzed data | This paper | GSE205022 |
| Ribosome Profiling/RNA seq raw and analyzed data | This paper | GSE199387 |
| Mass Spectrometry raw and analyzed data | This paper | PXD035621 |
| **Experimental models: Cell lines** | | |
| H9 (consent form available at https://hpscreg.eu/cell-line/WAe009-A) | WiCell | https://www.wicell.org/ |
| RC17 | Roslin Cells (provided by Agnete Kirkeby, Faculty of Health and Medical Sciences, University of Copenhagen, Denmark) | https://www.roslinct.com/ |
| HUES4 (consent form available at https://hpscreg.eu/cell-line/HVRDe004-A) | CSCB, University of Sheffield | https://www.sheffield.ac.uk/cscb |
| KOLF2.1 | Novo Nordisk Foundation Center for Stem Cell Medicine (reNEW), Faculty of Health and Medical Sciences, University of Copenhagen, Denmark (provided by Agnete Kirkeby) | N/A |
| **Experimental models: Organisms/strains** | | |
| CD1 (Mus musculus) mice | Charité University Hospital | CD1 mouse strain |
| **Oligonucleotides** | | |
| Full list in Table S7 | | |
| **Recombinant DNA** | | |
| pX335-U6-Chimeric_BB-CBh-hSpCas9n (D10A) (PX335) | Addgene | Cat# 42335 |
| pSpCas9(BB)-2A-GFP (PX458) | Addgene | Cat# 48138 |

(*Continued on next page*)

*Continued*

| REAGENT or RESOURCE | SOURCE | IDENTIFIER |
|---|---|---|
| pAAV-PuroCAG-EGFP | Bertero et al.[42] | N/A |
| M50 Super 8x TOPFlash | Addgene | Cat# 12456 |
| M51 Super 8x FOPFlash | Addgene | Cat# 12457 |
| Software and algorithms | | |
| Excel | Microsoft | https://www.microsoft.com/en-us/microsoft-365/excel |
| Graphpad Prism | GraphPad | https://www.graphpad.com/scientific-software/prism/ |
| R Studio (ggplot2, pheatmap packages) | Joseph J. Allaire | https://github.com/rstudio/rstudio |
| Image J | National Institutes of Health | https://imagej.net/ij/index.html |
| Illumina bcl2fastq | Illumina | https://emea.support.illumina.com/sequencing/sequencing_software/bcl2fastq-conversion-software/downloads.html |
| Cutadapt | Sven Rahmann | https://cutadapt.readthedocs.io/en/stable/https://doi.org/10.14806/ej.17.1.200 |
| bowtie2 (v2.2.9) | Ben Langmead | https://github.com/BenLangmead/bowtie2 |
| STAR | Alex Dobin | https://github.com/alexdobin/STAR |
| Ribotaper | Uwe Ohler | https://ohlerlab.mdc-berlin.de/software/RiboTaper_126/ |
| samtools | Heng Li | https://github.com/samtools/samtools |
| FeatureCounts | Yang Liao | https://subread.sourceforge.net/featureCounts.html#:~:text=featureCounts%20is%20a%20highly%20efficient,and%20genomic%20DNA%2Dseq%20reads. |
| Ribosomal Investigation and Visualization to Evaluate Translation (RIVET) | Amanda W. Ernlund et al.[43] | https://github.com/ruggleslab/rivet |
| WebGestalt | Developed by Liao et al.[44] | http://www.webgestalt.org/ |
| deepTools suite | Fídel Ramirez | https://github.com/deeptools/deepTools/ |
| WiggleTools | Ensembl | https://github.com/Ensembl/WiggleTools |
| wigToBigWig | Encode, kentUtils | https://www.encodeproject.org/software/wigtobigwig/ |
| Proteome Discoverer 2.4. TMT SPS-MS3 | Thermo Fisher | ====https://www.thermofisher.com/dk/en/home/industrial/mass-spectrometry/liquid-chromatography-mass-spectrometry-lc-ms/lc-ms-software/multi-omics-data-analysis/proteome-discoverer-software.html?gclid=Cj0KCQiAxbefBhDfARIsAL4XLRr4At2nNE2D6Lk_Q_jKdQSIVl-wotiUiIO2rqMx_xnd3dz6nqU2nCsaArQZEALw_wcB&cid=E.23CMD.DL103.12911.01&ef_id=Cj0KCQiAxbefBhDfARIsAL4XLRr4At2nNE2D6Lk_Q_jKdQSIVl-wotiUiIO2rqMx_xnd3dz6nqU2nCsaArQZEALw_wcB:G:s&s_kwcid=AL!3652!3!334040549172!p!!g!!proteome%20discoverer |
| DEqMS pipeline for TMT labelled MS data | Yafeng Zhu | https://github.com/yafeng/DEqMS |
| MacPyMol Version 2.1 INTEL-12.10.12 | Schrödinger platform | https://pymol.org/2/ |

(*Continued on next page*)

*Continued*

| REAGENT or RESOURCE | SOURCE | IDENTIFIER |
|---|---|---|
| Illumina bcl2fastq | Illumina | https://emea.support.illumina.com/sequencing/sequencing_software/bcl2fastq-conversion-software/downloads.html |
| Other | | |
| snoRNA database | Université de Toulouse | snorna.biotoul.fr |
| Ribosome structure | Reported by Khatter et al.[17] | https://www.rcsb.org/structure/4UG0 |
| Ribosome/FMRP structure | Reported by Chen et al.[41] | EMD-5806 on http://emsearch.rutgers.edu |

## RESOURCE AVAILABILITY

### Lead contact

Further information and requests for resources and reagents should be directed to and will be fulfilled by the lead contact, Anders H. Lund (anders.lund@bric.ku.dk).

### Materials availability

This study did not generate new unique reagents.

### Data and code availability

RMS data have been deposited at GEO and are publicly available as of the date of publication. Accession numbers are listed in the key resources table.

Ribosome profiling/RNA sequencing data has been deposited at GEO and are publicly available as of the date of publication. Accession numbers are listed in the key resources table.

Mass spectrometry data have been deposited at the ProteomeXchange Consortium via the PRIDE partner repository and are publicly available as of the date of publication. Accession numbers are listed in the key resources table.

This paper does not report original code.

Any additional information required to reanalyze the data reported in this paper is available from the lead contact upon request.

## EXPERIMENTAL MODEL AND STUDY PARTICIPANT DETAILS

### Animals

CD1 mouse (Mus musculus) lines were maintained in the animal facilities of the Charité University Hospital. All experiments were performed in compliance with the guidelines for the welfare of experimental animals approved by the State Office for Health and Social Affairs, Council in Berlin, Landesamt für Gesundheit und Soziales (LaGeSo), permission T0267/15 for post mortem tissue collection. Mice were housed in a 12 h/12 h light/dark cycle, at a consistent 18–23 °C, 40–60% humidity, with pellet food and water available ad libitum. Mice were used in the embryonic and postnatal period, with the stage and replicate numbers as reported for each experiment. Each sample was inclusive of both male and female sexes in each litter without distinction.

### Cell lines

Human embryonic stem cell (hESC) lines H9 (female), RC17(female), and HUES4 (male) were grown under feeder-free conditions on plates coated with hESC-qualified Matrigel (Corning Life Sciences, #354277) in mTeSR™1 medium (Stem Cell Technologies, #85850). Medium changes were performed daily. Cells were passaged about every three days using 1X TrypLE™ Select (Life Technologies, #12563-011) when reaching 80-90% confluence.

Upon thawing, Rock inhibitor (Y-27632) (LC laboratories, #Y-5301) was added at a final concentration of 10μM. Cells were frozen in half mTeSR™1 medium and half FBS-20% DMSO (final DMSO concentration: 10%).

KOLF2 iPS cells (male) were grown under feeder-free conditions on Matrigel-coated plates in TeSR™-E8™ (Stem Cell Technologies, #05990).

## METHOD DETAILS

### Cell culture

#### *Generation of neural progenitor cells*

H9 hESCs were differentiated into early neural progenitor cells (eNPCs) with STEMdiff™ Neural Induction Medium (Stem Cell Technologies, #05835) following the manufacturer's instructions for the monolayer protocol variant. In brief, H9 cells were plated on

Matrigel-coated plates at a density of $2x10^6$ cells per cm in neural induction medium supplemented with 10μM Rock inhibitor. Medium was changed every day and the cells passaged after about a week. After two more passages in neural induction medium, the cells were transferred into STEMdiff™ Neural Progenitor Medium (Stem Cell Technologies, #05833) for expansion, freezing, or further differentiation and maturation.

***Long-term neural differentiation***

H9-derived NPCs were further differentiated into late neural progenitor cells (lNPCs, or neural precursors, according to the manufacturer) by plating them at 125.000 cells/$cm^2$ on Matrigel and growing the cells in STEMdiff™ Neuron Differentiation Kit (Stem Cell Technologies, #08500) medium for one week with daily medium changes.

After one week, the cells were dissociated and plated at a density of $3x10^4$ cells/cm in STEMdiff™ Neuron Maturation Kit (Stem Cell Technologies, #08510) medium on a double layer of poly-L-ornithine (Sigma-Aldrich #P3655) at 15μg/mL in PBS and laminin (Sigma-Aldrich, #L2020) at 5μg/mL in DMEM/F-12. The medium was changed every second day and the cells kept in culture up to 52 days.

***Neural progenitor cell maintenance***

H9 hESC-derived early neural progenitor cells (eNPCs) were grown on Matrigel (Corning Life Sciences, #354277) in STEMdiff™ Neural Progenitor Medium (Stem Cell Technologies, #05833).

Cells were passaged around every five days at 80-90% confluence using Accutase (Stem Cell Technologies, #07920) for detaching and DMEM/F-12 + GlutMAX (Invitrogen, #31331-028) for resuspension, and frozen in STEMdiff™ Neural Progenitor Freezing Medium (Stem Cell Technologies, #05838).

***Directed ES differentiation into the three embryonic germ layers***

HUES4, H9, RC17, and KOLF2 iPS cells were differentiated into ecto-, endo-, and mesoderm using the STEMdiff™ Trilineage Differentiation Kit (Stem Cell Technologies, #05230) according to the manufacturer's instructions.

In brief, ES cells were plated on day 0 in technical triplicates in Matrigel-coated 6-well plates in either mTeSR™1 (HUES4, H9) or TeSR™-E8™ medium (KOLF2 iPS) supplemented with 10μM Rock inhibitor for endo- and mesoderm differentiation at $2.10^6$ cells per well for endoderm and $0{,}5.10^6$ cells per well for mesoderm. Cells destined for ectoderm differentiation were directly plated in ectoderm differentiation medium on day 0, supplemented with 10μM Rock inhibitor, at a density of $2.10^6$ cells per well. On day 1, medium was switched to the respective germ layer differentiation medium and changed on a daily basis until day 5 for endo- and mesoderm differentiation, and day 7 for ectoderm differentiation. Bright field images were taken every day and cells from every day of differentiation analyzed by RT-qPCR and immunohistochemistry.

***WNT pathway induction by GSK3 inhibition***

H9 and RC17 hESCs were cultured in mTeSR™1 medium under in the stem cell conditions described above. Medium was changed daily without or with the addition of 6μM of GSK3i (CHIR99021, Axon Medchem, #1386).

### RNA isolation from mouse brains

CD-1 mice were sacrificed at embryonic stages E11, E12.5, E14, E15.5, E17, P0 (neonates) and 6-7 months (adult). The brains were dissected in ice cold PBS in a cold room and snap-frozen on dry ice. RNA was extracted using TRIZOL-LS according to the manufacturer's instructions.

### RiboMeth-Seq

RiboMeth-seq library construction and sequencing were performed as previously described.[33,36] Triplicate libraries were produced for each cell line or condition analyzed and grown to ~70–80% confluence before collection. A portion of 5 μg of total RNA was used for input. RNA was partially degraded in alkali at denaturing temperatures. The 20–40-nucleotide fragments were purified by PAGE and linkers added using a system relying on a modified *Arabidopsis* tRNA ligase joining 2′,3′-cyclic phosphate and 5′-phosphate ends. The libraries were sequenced on the Ion Proton platform using the Ion PI™ Hi-Q™ OT2 200 Kit (Life technologies # A26434), Ion PI™ Hi-Q™ Sequencing 200 Kit (Life Technologies #A26433), and the Ion PI Chip Kit v.3 (Life Technologies, # A26770).

### RiboMeth-seq Data treatment

Data was analyzed as previously reported.[33,36] Briefly, sequencing reads were mapped to a corrected human rRNA reference sequence. To facilitate comparison with other studies, we have used the human rRNA sequence numbering according to snoRNABase throughout this study (snorna.biotoul.fr). An alignment table of these rRNA sequences is provided in Krogh et al.[36] RiboMeth-seq score (RMS score) represents the fraction of molecules methylated at each nucleotide position and is calculated by comparing the number of read-end counts at the queried position to six flanking positions on either side. Quantifications are performed in mouse on 41 sites in 18S, 66 in 28S and 2 in 5.8S and in human on 41 sites in 18S, 68 in 28S and 2 in 5.8S respectively, for which both RMS plus mass spectrometry evidence exists, and are reliably detected in at least one of cell lines examined in this study (Table S6). As to facilitate comparison, the human numbering is used both for mouse and human samples. The equivalence between mouse and human sites can be found in Table S6.

Statistically significant differences in RMS signatures between two cell lines or conditions were determined by pairwise comparison ($p<0.05$, two-tailed unpaired Welch's t test and $\geq 0.15$ difference in RMS score).

Heat-map representations were produced using the pheatmap function in R.

RMS data has been deposited to Gene Expression Omnibus (GEO), accession: GSE205022

## Generation of loss and gain of function mutants

### *Generation of SNORD52 knock-out clones by CRISPR-Cas9*

H9 *hESCs.* Two guides (sgRNAs) encompassing the human SNORD52 gene were designed: GGAGTGGACGTTAGAAAGGG and GGATACTTGGGTCTCCAGAA.

Both sgRNAS were cloned into pX335 and pX458 plasmids respectively. The plasmids were co-transfected into H9 hESC cells using the Amaxa 4D nucleofector (#AAF-1003B and #AAF-1003X) and the P3 Primary Cell 4D-Nucleofector X kit (Lonza, #V4XP-3024).

48h after transfection, the cells were single-cell sorted into Matrigel-coated 96-well plates for double GFP/Crimson fluorescence by FACS. Rock inhibitor (Y-27632) was added to mTESR-1 medium until the second medium change.

After about two weeks, colonies became visible and were screened for successful deletion using standard PCR (forward primer: CTCCCAGTGGAGCTGTTCTC, reverse primer: GGGGGAGATTCCAAACCTTA), the GoTaq Green master mix (Promega, #M7122), and running the amplification products on a 1% Agarose gel.

Candidate clones were further verified by DNA sequencing and expanded. A few CRISPR-negative clones – showing no deletion of SNORD52 but having undergone otherwise the exact same procedure – were also expanded and tested alongside the two SNORD52 KO clones.

*In RC17 hESCs*. Two guides (sgRNAs) encompassing the human SNORD52 gene were designed TGCAAAATAGGAGTACACTG and GGATACTTGGGTCTCCAGAA and cloned into the pX458 plasmid also encoding the Cas9 nuclease and a GFP reporter.

RC17 cells were transfected using Lipofecatmine™ 3000 Transfection Reagent (ThermoFisher Scientific #L3000001) according to the manufacturer's instructions and single-cell sorted into Matrigel-coated 96-well plates for GFP fluorescence by FACS. Rock inhibitor (Y-27632) was added to mTESR-1 medium until the second medium change. Clone selection and verification was undertaken as for the H9 cells, using the following primers for PCR:

forward primer: CGTATTTTTGTTAAAGGCTGGG and reverse primer: CAAGGTGAAAACAAGACAATTTGA.

### *Generation of SNORD52 overexpression clones*

The SNORD52 gene sequence was cloned into an artificial intron and placed into a 2-exon EGFP sequence derived from pGINT (courtesy to Cristian Bellodi), subsequently used to replace the intron-less EGFP of the AAVS1-targeting vector pAAV-PuroCAG-EGFP obtained from Ludovic Vallier.

Following the protocol described in Bertero et al.,[42] the EGFP-SNORD52 construct was targeted to the AAVS1 safe harbor locus in H9 hESCs *via* zinc finger nucleases. As a control, the original pAAV-PuroCAG-EGF construct was used.

H9 hESCs were transfected with the Amaxa 4D Nucleofector. The cells were expanded for a few days, allowing for the elimination of transient transfection, then single cell FACS-sorted for GFP fluorescence. Correct insertion of the construct into the AAVS1 locus was verified by DNA sequencing, and SNORD52 expression by RT-qPCR.

## Gene expression

### *RNA isolation*

Total RNA preparation was performed using QIAZOL (Qiagen) and chloroform according to the protocol from the manufacturer. Concentrations were measured using a NanoDrop® ND-1000 UV-Vis and NanoDrop® One spectrophotometer (Thermo Scientific).

RNA size distribution and quality were assessed by automated electrophoresis using an Agilent 2100 Bioanalyzer system with the Agilent RNA 6000 Nano kit according to the manufacturer's instructions.

### *cDNA generation and RT-qPCR*

Reverse-transcription to cDNA was achieved with the TaqManReverese Transcription Kit (Applied Biosystems, #N80803234) according to the manufacturer's recommendations. Typically, 1μg of RNA was used per reverse transcription reaction.

RT-qPCR analyses were performed in technical triplicates on a StepOnePlus™ Real-Time PCR System (Thermo Fisher Scientific, #4376600) in a 96-well format and using the Fast SYBR Green Master Mix (Thermo Fisher Scientific, #4385612). 2μL of cDNA were combined with 5μL of Fast SYBR Green Master Mix, 0.3μL of forward or reverse primer at 100μM, and 2.4μL nuclease-free water per well.

See Table S7 for the complete list of primers used in this study.

### *RT-qPCR data analysis*

Values were normalized either to GAPDH (mRNA) or SNORD46 (snoRNAs).

For the generation of heatmaps, all shown samples were additionally normalized along the range of values for each gene in order to fit them onto a scale from 0-100% (blue to red) in order to account for the differences in the magnitude of expression levels between different genes.

### *Immunofluorescence*

Cells were plated in Lab-Tek Chamber slides (Sigma Aldrich, #C7182) at the densities corresponding to the relevant protocol, washed with PBS and fixed for 15 minutes at RT with 4% paraformaldehyde, followed by three PBS washes and potential storage in PBS at 4°C.

Fixed cells were permeabilized for 10 minutes in PBS, 0.1% Triton, then incubated for 1h in blocking buffer (PBS, 5% FBS). Primary antibodies were diluted in blocking buffer at the indicated dilutions and left overnight at 4°C under gentle shaking, then washed off by applying PBS 3 times for 10 minutes. Secondary antibodies were diluted at a 1:1000 dilution in blocking buffer and left for 1h at room temperature. Slides were subsequently washed 3 times with PBS for 10 minutes and mounted in Duolink in situ mounting medium with DAPI (Sigma-Aldrich, #DUO82020-5ML).

Images were acquired with a Zeiss Axio Imager.M2 microscope (#490020-0004-000) and images analyzed with the open-source ImageJ software (Fiji).

Please consult the key resources table for the list of primary and secondary antibodies.

#### *Western Blotting*

Western blotting was performed as previously described.[73] See key resources table for the list of antibodies used.

## 3D MODELLING

Modelling performed using MacPyMol (Version 2.1 INTEL-12.10.12) on the structure 4UG0 (https://www.rcsb.org/structure/4UG0) published by Khatter et al.[17] for the FMRP part:

Structure published by Chen et al.[41] Accession number: EMD-5806 on http://emsearch.rutgers.edu.

## Ribosome profiling

#### *Ribosome profiling*

Ribosome Profiling was performed essentially as previously described,[74] following the protocol given in TruSeq Ribo Profile Mammalian (Illumina), with minor modifications. Three individual replicates for each of the two cell lines were collected. A single 15cm dish corresponding to one replicate was harvested at a time. For each replicate, cell media was aspirated and cells washed with ice-cold PBS. No cycloheximide pre-treatment was performed. After thorough removal of the PBS, the dish was fully immersed in liquid nitrogen and placed on dry ice. For cell lysis, 1mL of 1x Mammalian Lysis Buffer (Illumina) containing 100 μg/mL cycloheximide was added dropwise to the dish which was then placed on wet ice. Cells were then scraped off to the lower portion of the dish and allowed to thaw in the lysis buffer. Lysate was homogenized by pipetting and triturated ten times through a 25-gauge needle. The lysate was then transferred to a DNA LoBind 1.5mL microfuge tube (Eppendorf) and incubated on ice for 5min. The lysate was cleared by centrifugation at 20000g, 4°C for 10min and the supernatant transferred to a fresh microfuge tube. Aliquots were prepared for each replicate, flash-frozen in liquid nitrogen and stored at -80°C until further use. The steps detailed in TruSeq Ribo Profile Mammalian protocol (Illumina) were followed to generate total RNA and ribosome protected fragment (RPF) RNAseq libraries corresponding to the 3 individual replicates from each of the two cell lines. For RPFlibraries, following nuclease digestion, monosomes were purified using illustra MicroSpin S-400 HR Columns. Ribo-Zero™ Gold Kit (Illumina) was used to deplete ribosomal rRNA. The libraries prepared from total RNA or RPF for both conditions were pooled and sequenced on a NextSeq® 500 System (Illumina).

#### *Ribosome Profiling data analysis*

The sequencing data was demultiplexed using Illumina bcl2fastq. Quality of the sequencing files were controlled with fastqc. Adaptor sequences were removed with cutadapt. Reads derived from RPF and total RNA were aligned to human rRNA and tRNA sequences with bowtie2 (v2.2.9) and the mapped reads discarded. The remaining reads were aligned to GRCh38.p12 (Ensembl v.97) with STAR. Reads mapping to Human Genome Organisation (HUGO) approved genes were used for downstream analyses. RPF read lengths were analyzed for trinucleotide periodicity as described previously[35]. RPF read alignment files were filtered with samtools to retain only 28 to 31nt read lengths. No read length filtering was applied to the total RNA alignment files. The optimal P-site offset for size selected RPF aligned reads was defined as position 12 from 5' read ends. A single canonical transcript representing each protein-coding gene was selected from the GRCh38, v97 Ensembl annotation file according to criteria previously described[35] (Table S6). FeatureCounts was used to generate counts of primary reads mapping to exons of these transcripts for both total RNA and RPF. RPF reads with ribosome P-site positions mapping within transcript coding-region sequences (CDS) were again counted using FeatureCounts, and along with the mRNA exons mapped reads, used for further measurements of differential translation and mRNA expression. Ribosomal Investigation and Visualization to Evaluate Translation (RIVET),[43] was used for translation and expression analysis of the representative transcripts (similar results were obtained for gene-level analysis). No fold-change cut-offs were directly applied, in order to additionally detect more subtle changes in translation. Regulated transcripts were therefore nominally identified by statistical significance. Translation regulation categories were defined according to RIVET, based on mRNA expression and ribosome occupancy, derived from normalized total RNA read counts or RPF read counts mapping to protein-coding mRNA transcripts, respectively (Table S4). Plots from the resulting RIVET output files were generated using the ggplot2 package in R. The RNA sequencing data has been deposited to GEO, accession: GSE199387.

#### *RNA-seq differential expression analysis*

The raw RNA-seq read count table was imported into R. For each pairwise analysis, appropriate columns from the read count table were selected and an intercept design matrix was created using the model.matrix function. The read count matrix was then converted into a DGEList object using the EdgeR package and rows that consistently have zero or very low counts were removed using the filterByExpr function. Normalization for library sizes was then applied using the calcNormFactors function from EdgeR (method="TMM"). The normalized count data was then transformed for linear modelling using the voom function from the Limma package. Linear model fitting was then performed using the lmFit function from Limma. Statistical analysis was performed using the eBayes function from Limma. Plots from the resulting output files were generated using the ggplot2 package in R. For analysis of total RNA libraries from H952KO and H9WT the raw FeatureCounts table described above was used as input. For the analysis of published data from haploid H9 human embryonic stem cells and their differentiation into neuroectoderm, early mesoderm, and definitive endoderm,[46] the raw RNA-seq read count table was obtained from the GEO database (GEO accession: GSE143371). For each of the three differentiation types, the appropriate columns were selected from the read count table (Empty.vector_Neuroectoderm_rep_1-3;

Empty.vector_Early_Mesoderm_rep_1-3; Empty.vector_Definitive_Endoderm_rep_1-2) and a read count matrix constructed together with the undifferentiated control samples (Empty.vector_Undifferentiated_rep_1-3) in each case.

### *Gene ontology and gene-set enrichment analysis*

All Gene ontology (GO) analyses of RNA-seq and ribosome profiling data was performed using the WebGestalt using the over-representation test against GO biological process database (genome protein coding),[44] with parameters: minimum number of genes for a category = 10; Maximum number of genes for a category = 500; Multiple Test Adjustment = BH.

### *Metagene analysis*

For metagene analyses, bam files containing exon-mapped reads for each library were converted to normalized reads per kilobase per million (RPKM) or counts per million reads (CPM) single-nucleotide resolution coverage bigwig files, with bamCoverage from the deepTools suite. WiggleTools (Ensembl) and wigToBigWig (Encode, kentUtils) were then used to merge these and create mean coverage files per condition. These were input to deepTools computeMatrix, together with an annotation file containing the exon coordinates for the selected mRNA transcripts. For RPF coverage over all transcripts, a count matrix was then generated for library RPKM RPF coverage over the coding regions (CDS), scaled to size 100 nt, flanked by unscaled regions before and after the translation start (TSS) and end (TES) sites. For further analysis, the scaled coverages of transcripts comprising the different translationally regulated categories were extracted from this matrix and median values at each position plotted. For average ribosome occupancy, CPM normalization was used and offset applied using bamCoverage, so as to use only the nucleotide position representing the ribosome P-site for each read as the signal (see 'ribosome profiling data analysis', above). The P-site coverage files were input to computeMatrix and a count matrix generated for −30 to +330 or −330 to +30 nucleotides, relative to the CDS start or end site respectively for each transcript (unscaled). The resulting counts at each position were divided by the total RPF count in CDS for each corresponding transcript to give the average ribosome occupancy per nucleotide position in each transcript. The mean values at each equivalent nucleotide position relative to the translation start site were plotted after extreme outlier removal (>3x interquartile range), no smoothing was applied. For P-site CPM the same matrices were used, although here the counts at each position were summed at each nucleotide position. For plotting, extreme outliers (>3x interquartile range) were removed. Plots were produced using ggplot2 in R.

### Global nascent peptide synthesis assay

Global novel protein synthesis was assessed using the Click-iT Plus OPP Protein Synthesis Assay Kit (Life Technologies, #C10456 for green fluorescence, #C10457 for red fluorescence given that the overexpression clones are constitutively expressing EGFP) according to the manufacturer's protocol.

### TOP/FOP Wnt reporter assay

The M50 Super 8x TOPFlash (Addgene #12456) and M51 Super 8x FOPFlash (Addgene, #12457) were transfected together with a pRLTK (Renilla) plasmid using the Mirus2020 transfection reagent (MirusBio, #MIR 5404) according to the supplier's protocol in a 12-well plate format in technical triplicates.

Cells were prepared for Luciferase and Renilla measurements using the Dual-Glo Luciferase Assay System (Promega, #E2920) according to the manufacturer's instructions. Luminescence readings were carried out on a GloMax Multi Detection System (Promega). Luciferase readings were normalized to the corresponding Renilla values.

### Northern blotting analysis of rRNA processing

Total RNA (7.5 μg) was separated on a formaldehyde denaturing 1% agarose gel and transferred to a BrightStar-Plus membrane (Ambion) using capillary blotting followed by UV cross-linking. The probes (10 pmol each) were radiolabelled with [γ-32P]ATP using T4 PNK (Thermo Scientific) and hybridized to the membrane overnight in hybridization buffer (4× Denhardt's solution, 6× SSC, 0.1% SDS) at Tm of the probe of −10 °C. The membrane was subsequently washed four times in 3× SSC supplemented with 0.1% SDS, followed by exposure to a propidium iodide screen and scanned on a Typhoon scanner (GE Healthcare).

### Mass spectrometry on 80S and polysomes

Proteins from polysome profile fractions containing 80S ribosomes and polysomes respectively, were precipitated with 20% Trichloroacetic Acid and washed three times in ice cold acetone. Protein pellets were solubilized using 100 μl of lysis buffer (50 mM HEPES (pH 8.5), 6 M guanidinium hydrochloride, 10 mM TCEP, 40 mM CAA). Samples were boiled at 95°C for 5 min., after which they were sonicated on high for 5×30 sec. in a Bioruptor sonication water bath (Diagenode) at 4°C. After determining protein concentration with Bradford (Sigma), 10 μg was taken forward for digestion. Samples were diluted 1:3 with 10% Acetonitrile, 50 mM HEPES pH 8.5, LysC (MS grade, Wako) was added in a 1:50 (enzyme to protein) ratio, and samples were incubated at 37°C for 4 hrs. Samples were further diluted to 1:10 with 10% Acetonitrile, 50 mM HEPES (pH 8.5), trypsin (MS grade, Promega) was added in a 1:100 (enzyme to protein) ratio and samples were incubated overnight at 37°C. Enzyme activity was quenched by adding 2% trifluoroacetic acid (TFA) to a final concentration of 1%. Prior to TMTPro labeling, the peptides were desalted on in-house packed C18 Stagetips.[16] For each sample, 2 discs of C18 material (3M Empore) were packed in a 200ul tip, and the C18 material activated with 40 μl of 100% Methanol (HPLC grade, Sigma), then 40 μl of 80% Acetonitrile, 0.1% formic acid. The tips were subsequently equilibrated 2× with 40 μl of 1% TFA, 3% Acetonitrile, after which 10 μg of sample was loaded using centrifugation at 4,000 rpm. After washing the tips twice with 100 μl of 0.1% formic acid, the peptides were eluted into clean 500 μl Eppendorf tubes using 40% Acetonitrile, 0.1% formic acid. The eluted peptides were concentrated in an Eppendorf Speedvac, and re-constituted in

50 mM HEPES (pH 8.5) for TMTPro labeling. For normalization, an equimolar peptide mix from all the samples was generated by mixing equal amounts from each sample, that could subsequently act as a normalization spike-in. Labeling was done according to manufacturer's instructions, and subsequently, labeled peptides were mixed 1:1:1:1:1:1:1:1:1:1:1:1:1:1:1 (13-plex, 12 samples + 1 normalization spike-in), acidified to 1% TFA and Acetonitrile concentration brought down to <5% using 2% TFA. Prior to mass spectrometry analysis, the peptides were fractionated using an offline ThermoFisher Ultimate3000 liquid chromatography system using high pH fractionation (5mM Ammonium Bicarbonate, pH 10) at 5 μl/min flowrate. 10 μg of peptides were separated over a 70 min. gradient (5% to 35% Acetonitrile), while collecting fractions in 204 sec. intervals. The resulting 20 fractions were pooled into 10 final fractions and vacuum concentrated to dryness. Fractions were resuspended in 1% TFA, 2% Acetonitrile for MS analysis.

### MS data acquisition

For each fraction, peptides were loaded onto a C18 trap cartridge (ThermoFisher 160454), connected in-line to a 50 cm C18 reverse-phase analytical column (Thermo EasySpray ES803) using 100% Buffer A (0.1% Formic acid in water) at 5 μl/min., using the Ultimate3000 HPLC system. After trap loading, the sample loop was switched out of the flowpath, and peptides were eluted over a 90 min. method ranging from 8% to 60% of Buffer B (80% acetonitrile, 0.1% formic acid) at 200 nl/min. The Orbitrap Fusion instrument (Thermo Fisher Scientific) was run in an SPS MS3 top speed method with FAIMSPro ion mobility enabled (2 CVs, -50V and -70V). Full MS spectra were collected at a resolution of 120,000, with an AGC target of 100% or maximum injection time of 50 ms and a scan range of 400–1600 m/z. The MS2 spectra were obtained in the ion trap operating at turbo speed, with an AGC target value of $1\times10^4$ or maximum injection time of 35 ms, a normalised CID collision energy of 35 and an intensity threshold of 5e3. Dynamic exclusion was set to 60 s, and ions with a charge state <2, >6 or unknown were excluded. From the resulting MS2 scan, 10 precursors were selected for SPS-MS3 analysis, fragmented with a normalised HCD collision energy of 55, and ions collected for a maximum of 118 ms or AGC target of 250%. Resulting MS3 spectra were collected at 60,000 resolution and scan range of 100–500 for reporter ion quantification. FAIMS CVs were switched on the fly, with 1.5 s cycle time dedicated to each CV. MS performance was verified for consistency by running complex cell lysate quality control standards, and chromatography was monitored to check for reproducibility. The mass spectrometry data have been deposited to the ProteomeXchange Consortium (http://proteomecentral.proteomexchange.org) via the PRIDE partner repository with the dataset identifier **PXD035621**.

### TMT Quantitative Proteomics Analysis

The raw files were analyzed using Proteome Discoverer 2.4. TMT SPS-MS3 quantitation was enabled in the processing and consensus steps, and spectra were matched against the 9606 Human database obtained from UniProt. Dynamic modifications were set as Oxidation (M), Deamidation (N,Q) and Acetyl on protein N-termini. Cysteine carbamidomethyl and TMTPro were set as static modifications on peptide N-termini and Lysine residues. All results were filtered to a 1% FDR, and protein quantitation done using the built-in Minora Feature Detector.

### Proteomic mass spectrometry data analysis

All MS spectra were searched in Proteome Discoverer 2.4 (ThermoFisher), using the SEQUEST algorithm against the human proteome Uniprot database (containing its reversed complement and known contaminants). Spectral matches were filtered to false discovery rate (FDR) <0.01, using the target-decoy strategy combined with linear discriminant analysis. Proteins were quantified only from peptides with an Average Reporter S/N Threshold of 10, and co-isolation specificity of 0.75.

To examine only those proteins most likely to be truly ribosome associated, thus eliminating proteins likely to be contaminants throughout the sucrose gradients, identified proteins were filtered against a complied list of previously identified high confidence 40S/60S interacting proteins (Table S5).

Statistical analyses of protein abundance changes were performed using the DEqMS pipeline for TMT labelled MS data (https://github.com/yafeng/DEqMS), with q.value<0.05. Log2FC changes in protein abundance were determined to be significant at sca.adj.pval (Benjamini-Hochberg method adjusted DEqMS p-values) <0.05 (Table S5). The abundance values scaled to the reference channel (pooled sample) output from Proteome Discoverer were used as input.

Volcano plots for each comparison were generated using the ggplot2 package in R. Bar charts were generated in Graphpad Prism using DEqMS normalized abundances and statistical significance was tested using two-tailed unpaired Welch's *t* test.

The mass spectrometry data have been deposited to the ProteomeXchange Consortium, via the PRIDE repository with the dataset identifier PXD035621.

## QUANTIFICATION AND STATISTICAL ANALYSIS

The statistical details for every experiment (number of replicates, nature of statistical tests, and meaning of symbols used to signal significance) are detailed in the figure legends. Each experiment used 3 or more biological replicates, and values are presented as mean ± SD, unless otherwise indicated in the figure legends. Statistical differences between samples were determined by Welch's unpaired t-test unless otherwise indicated. Values of $p < 0.05$ were considered statistically significant unless stated otherwise.

Basic statistical analyses were carried out using the Excel and Graphpad Prism software and plotted either in Graphpad Prism or in R Studio using the ggplot2 and the pheatmap packages.